Complex conductivity of volcanic rocks and the geophysical mapping of alteration in volcanoes

A. Ghorbani, A. Revil, A. Coperey, A Soueid Ahmed, S. Roque, M.J. Heap, H. Grandis, F. Viveiros, A. Soueid Ahmed

Journal of Volcanology and Geothermal Research 357 (2018) 106–127

Contents lists available at ScienceDirect

Journal of Volcanology and Geothermal Research

journal homepage: www.elsevier.com/locate/jvolgeores

Complex conductivity of volcanic rocks and the geophysical mapping of alteration in volcanoes

A. Ghorbani [a], A. Revil [b,*], A. Coperey [b], A. Soueid Ahmed [b], S. Roque [b], M.J. Heap [c], H. Grandis [d], F. Viveiros [e]

[a] Department of Mining and Metallurgical Engineering, Yazd University, Yazd, Iran
[b] Univ. Grenoble Alpes, Univ. Savoie Mont Blanc, CNRS, IRD, IFSTTAR, ISTerre, 38000 Grenoble, France
[c] Géophysique Expérimentale, Institut de Physique de Globe de Strasbourg, UMR 7516 CNRS, Université de Strasbourg/EOST, Strasbourg Cedex, France
[d] Applied and Exploration Geophysics Group, Faculty of Mining and Petroleum Engineering, Institut Teknologi Bandung (ITB), Bandung, Indonesia
[e] Instituto de Investigação em Vulcanologia e Avaliação de Riscos, Universidade dos Açores, Ponta Delgada, Portugal

ARTICLE INFO

Article history:
Received 23 February 2018
Received in revised form 16 April 2018
Accepted 17 April 2018
Available online 22 April 2018

ABSTRACT

Induced polarization measurements can be used to image alteration at the scale of volcanic edifices to a depth of few kilometers. Such a goal cannot be achieved with electrical conductivity alone, because too many textural and environmental parameters influence the electrical conductivity of volcanic rocks. We investigate the spectral induced polarization measurements (complex conductivity) in the frequency band 10 mHz–45 kHz of 85 core samples from five volcanoes: Merapi and Papandayan in Indonesia (32 samples), Furnas in Portugal (5 samples), Yellowstone in the USA (26 samples), and Whakaari (White Island) in New Zealand (22 samples). This collection of samples covers not only different rock compositions (basaltic andesite, andesite, trachyte and rhyolite), but also various degrees of alteration. The specific surface area is found to be correlated to the cation exchange capacity (CEC) of the samples measured by the cobalthexamine method, both serving as rough proxies of the hydrothermal alteration experienced by these materials. The in-phase (real) conductivity of the samples is the sum of a bulk contribution associated with conduction in the pore network and a surface conductivity that increases with alteration. The quadrature conductivity and the normalized chargeability are two parameters related to the polarization of the electrical double layer coating the minerals of the volcanic rocks. Both parameters increase with the degree of alteration. The surface conductivity, the quadrature conductivity, and the normalized chargeability (defined as the difference between the in-phase conductivity at high and low frequencies) are linearly correlated to the CEC normalized by the bulk tortuosity of the pore space. The effects of temperature and pyrite-content are also investigated and can be understood in terms of a physics-based model. Finally, we performed a numerical study of the use of induced polarization to image the normalized chargeability of a volcanic edifice. Induced polarization tomography can be used to map alteration of volcanic edifices with applications to geohazard mapping.

1. Introduction

Geophysical methods and the methods developed in the framework of hydrogeophysics are increasingly used on volcanoes to determine the distribution of material properties (e.g., seismic velocities, bulk density, electrical properties) with application to volcanic eruption forecasting, geohazard mapping, and hydrogeology. Electrical conductivity tomography can be used to image the 3D distribution of the electrical conductivity of volcanoes (e.g., Johnson et al., 2010; Revil et al., 2010; Rosas-Carbajal et al., 2016; Gresse et al., 2017). Electrical conductivity of volcanic rocks depends on two contributions. The first is a bulk contribution controlled by the water content and pore water salinity. It corresponds to electrical conduction through the connected pore network of the material (e.g., Archie, 1942). The second contribution is an interfacial contribution called surface conductivity. This contribution is associated with conduction in the electrical double layer coating the mineral grains (e.g., Revil et al., 2002 for volcanic rocks and Waxman and Smits, 1968 for sedimentary materials). This electrical double layer consists of the Stern layer (with weakly or strongly adsorbed counterions depending on their affinity for the mineral surface) and the diffuse layer. Since electrical conductivity of volcanic rocks depends on these two contributions, electrical conductivity tomography is rather difficult to interpret and therefore cannot be used as a stand-alone geophysical method (see discussion in Bernard et al., 2007; Komori et al., 2010; Kemna

* Corresponding author.
E-mail addresses: aghorbani@yazd.ac.ir (A. Ghorbani), andre.revil@univ-smb.fr (A. Revil), antoine.coperey@gmail.com (A. Coperey), abdellahii@yahoo.com (A. Soueid Ahmed), roquesandra@hotmail.fr (S. Roque), heap@unistra.fr (M.J. Heap), grandis@geoph.itb.ac.id (H. Grandis), Maria.FB.Viveiros@azores.gov.pt (F. Viveiros).

https://doi.org/10.1016/j.jvolgeores.2018.04.014
0377-0273/

et al., 2012; Usui et al., 2016; Soueid Ahmed et al., 2018a, 2018b). For instance, a volcano can be a highly conductive body because of the high salinity of the pore water or a high degree of alteration (or both). Induced polarization can be used to discriminate these effects as long as the content in metallic particles (e.g., pyrite and magnetite) is not too high (i.e., 1% in vol.).

In the context of the present paper, it may be useful to recall what we mean by alteration. Classically, the alteration of volcanic rocks is produced by the circulation of hydrothermal fluids and involves the replacement of primary igneous glass and minerals (e.g., plagioclase, pyroxene, amphibole) by secondary minerals that are stable at the thermodynamic conditions of alteration (e.g., Bonnet and Corriveau, 2007). We are especially interested by the case where these secondary minerals are clay minerals (kaolinite, chlorite, illite, and smectite, see Honnorez et al., 1998). Note that some volcanic rocks can also be altered through surface weathering.

Complex conductivity characterizes the reversible storage of electrical charges in rocks (Schlumberger, 1920; Bleil, 1953; Seigel, 1959), a process known as (induced) polarization. This "polarization" is a low frequency (<10 kHz) characteristic of rocks that is unrelated to the dielectric polarization phenomena observed at higher frequencies (>10 kHz) (e.g., Revil, 2013). The origin of the low-frequency polarization of rocks is generally associated with the polarization of the electrical double layer around the mineral grains and can be described with two interrelated parameters: the quadrature conductivity and the normalized chargeability (see Revil et al., 2017b). The quadrature conductivity corresponds to the imaginary component of the complex conductivity. The normalized chargeability measures the dispersion of the in-phase conductivity with the frequency. Since the polarization and surface conductivity are both controlled by the properties of the electrical double layer, it is therefore unsurprising that these parameters are also interrelated (Revil et al., 2017b). This relationship is very important to interpret electrical resistivity and induced polarization tomographies that can be carried out at the scale of volcanic structures. As a side note, measurements of induced polarization can be performed in the field with the same equipment used for electrical resistivity tomography (e.g., Kemna et al., 2012). Induced polarization may therefore appear as an attractive method to study volcanic and geothermal systems.

The key questions we want to address are (1) Is the relationship developed in a previous paper for basaltic rocks (Revil et al., 2017a) valid for all types of volcanic rocks? (2) Is the cation exchange capacity (CEC) a proxy of the alteration of the volcanic rocks? (3) How do the surface and quadrature conductivities of volcanic rocks depend on their cation exchange capacity (CEC) and specific surface area? (4) How can the quadrature conductivity and the normalized chargeability be related to each other? (5) How is the polarization affected by temperature and the volume content of metallic particles? (6) Can we image electrical conductivity and normalized chargeability of a volcanic edifice and offer a combined approach to interpret these data? Answers to these questions are important to use induced polarization tomography to image the alteration of volcanic rocks. Since alteration is responsible for the weakening of the mechanical properties of volcanic rocks (see Pola et al., 2012; Frolova et al., 2014; Wyering et al., 2014; Heap et al., 2015), our study has strong implications regarding the mapping of geohazards in volcanic environments (Day, 1996; Reid et al., 2001; Finn et al., 2001; Reid, 2004).

We investigate here the complex conductivity of a set of 85 new core samples from five active volcanoes in the world: Merapi and Papandayan in Indonesia, Furnas in Portugal, Yellowstone in the USA, and Whakaari (White Island) in New Zealand. The laboratory measurements were collected in the frequency range 10 mHz–45 kHz with a very sensitive impedance meter. The interpretation of the laboratory data will be based on the dynamic Stern layer polarization model developed in Revil (2013) and recently updated in Revil et al. (2017a, 2017b, 2018).

2. Theory

2.1. The dynamic stern layer model

The (in-phase) conductivity of a volcanic rock represents its ability to carry electrical current. A volcanic rock can also reversibly store electrical charges (Revil et al., 2017c), a phenomenon known as polarization. This polarization is responsible for a phase lag between the electrical current and the electrical field for frequency-domain measurements (Kemna et al., 2012) or a secondary voltage for time-domain measurements (Schlumberger, 1920). The polarization phenomenon is represented both by a quadrature (imaginary) component of the complex electrical conductivity and by a dispersion of the in-phase conductivity with the frequency. The high frequency conductivity σ_∞ is the instantaneous conductivity of a material once electromagnetic diffusion has fully occurred. Conversely, the conductivity σ_0 is the Direct Current (DC) conductivity obtained once all the polarization phenomena are fully established. Some of the charge carriers are blocked at the end of the polarization length scales and do not participate anymore to the conduction (Fig. 1). Obviously, we have $\sigma_0 \le \sigma_\infty$ and $\sigma_0 = \sigma_\infty(1 - M)$ where M (dimensionless) denotes the chargeability of the material (Fig. 1). The polarization is also described by a distribution of relaxation times associated with the polarization of a distribution of length scales (pore sizes or grain sizes). The main relaxation time of the problem τ corresponds to the time, once the primary electrical field or current is stopped, required for the accumulated charge carriers to return to their equilibrium state (in a statistical sense) (Fig. 1).

In the following, a harmonic external electrical field of the form $\mathbf{E} = \mathbf{E}_0 \exp(+i\omega t)$ is applied to a volcanic rock. In the realm of the dynamic Stern layer model, the complex conductivity $\sigma^* = \sigma' + i\sigma''$ of a porous granular material without metallic grains is then given by (Revil, 2013; Revil et al., 2014; Revil et al., 2017a, 2017b),

$$\sigma^*(\omega) = \sigma_\infty \left(1 - M \int_0^\infty \frac{h(\tau)}{1 + (i\omega\tau)^{1/2}} d\tau\right) + i\omega\varepsilon_\infty, \tag{1}$$

where i denotes the pure imaginary number, σ' denotes the in-phase conductivity (real component, a positive quantity), σ'' denotes the quadrature conductivity (imaginary component, a negative quantity), ε_∞ (in F m^{-1} = A s V^{-1} m^{-1}) corresponds to the permittivity associated with the Maxwell-Wagner polarization, ω denotes the angular frequency (rad s^{-1}), τ is a time constant (in s), and $h(\tau)$ denotes a (normalized) probability density for distribution of the time constants of the material, and $M = (\sigma_\infty - \sigma_0)/\sigma_\infty$ is the (dimensionless) chargeability. In first approximation, the electrical circuit shown in Fig. 2 can be used to provide some understanding of the conduction/polarization mechanisms occurring in a volcanic rock.

The expressions of the high and low frequency conductivities of a volcanic rock (see Fig. 1 for the underlying physics) can be obtained through a volume averaging method. According to Revil (2013), they are given by

$$\sigma_0 = \frac{1}{F}\sigma_w + \left(\frac{1}{F\phi}\right)\rho_g \beta_{(+)}(1-f)\mathrm{CEC}, \tag{2}$$

$$\sigma_\infty = \frac{1}{F}\sigma_w + \left(\frac{1}{F\phi}\right)\rho_g \left[\beta_{(+)}(1-f) + \beta^S_{(+)} f\right]\mathrm{CEC}. \tag{3}$$

In these equations, σ_w (in S m^{-1}) denotes the pore water conductivity (proportional to the salinity in isothermal conditions), ϕ denotes the (connected) porosity, F (dimensionless) the intrinsic formation factor, f (dimensionless) denotes the partition coefficient (fraction of counterions in the Stern layer versus the concentration of counterions populating entire double layer), ρ_g is the grain density (typically 2800–3100 kg m^{-3}), and CEC denotes the cation exchange capacity of the material (in C kg^{-1}).

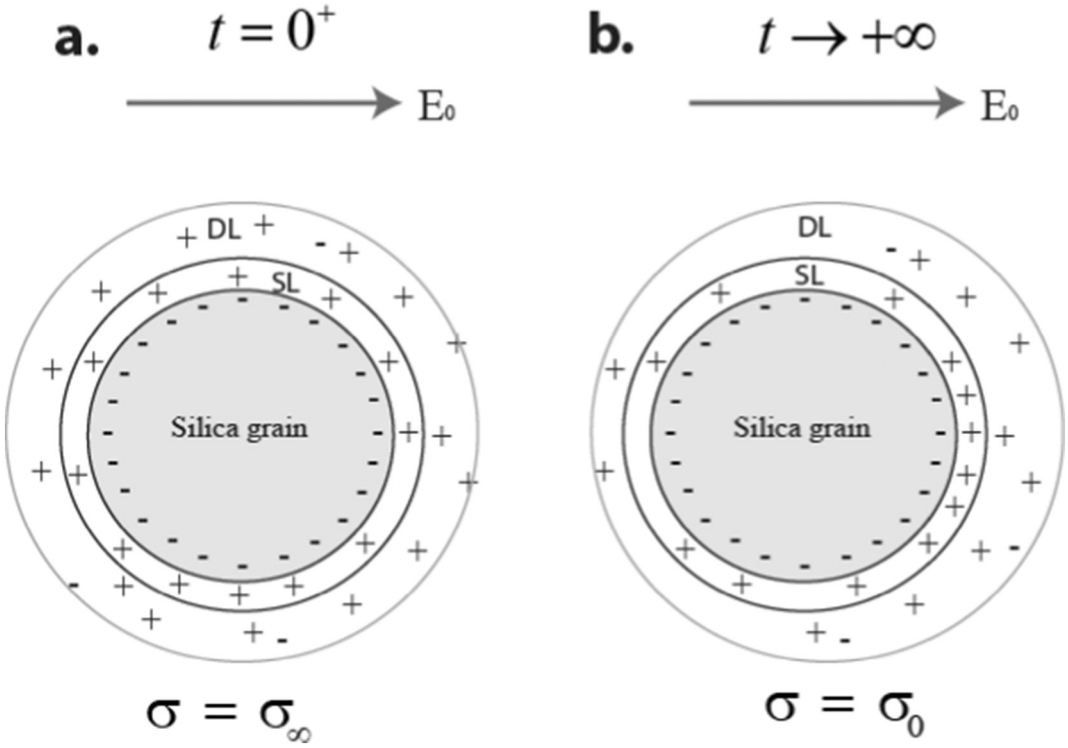

Fig. 1. Polarization of a grain coated by an electrical double layer composed by a diffuse layer (DL) and a Stern layer (SL) mobile along the surface of the solid phase of a volcanic rock. a. Just after the application of the primary electrical field $\mathbf{E}_0$, all the ionic charge carriers are mobile. The instantaneous conductivity is denoted as σ_∞. b. If the primary electrical field is applied for a long time, the conductivity is $\sigma_0 = \sigma_\infty(1 - M)$ where M stands for the chargeability of the material (dimensionless). Some of the charge carriers (those of the Stern layer) are now blocked at the edge of the grain in the direction of the electrical field. As the result, the conductivity of the material is reduced. The quadrature conductivity is proportional to the normalized chargeability defined as $M_n = \sigma_\infty - \sigma_0$.

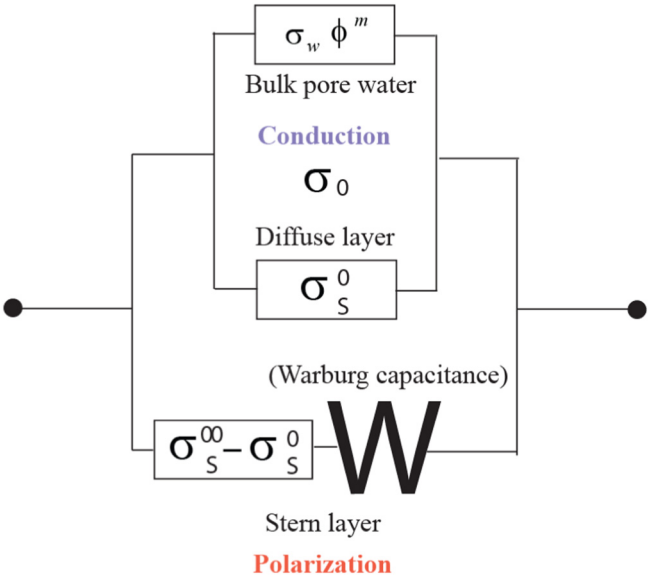

Fig. 2. Equivalent electrical circuit of a volcanic rock. The conduction process itself can be modeled, in first approximation, as two resistances in parallel. The first corresponds to the conduction in the bulk pore water. The second is associated with conduction in the electrical double layer. The Stern layer provides another additional conductivity and is responsible for the polarization of the material. The Warburg capacitance is used to model the Stern layer as a leaking capacitance. The quantity $F = \phi^{-m}$ denotes the intrinsic formation factor. The normalized chargeability is defined as $M_n = \sigma_\infty - \sigma_0 = \sigma_S^\infty - \sigma_S^0$ where the quantities σ_S^∞ and σ_S^0 denotes the instantaneous and DC surface conductivities, respectively. A volcanic rock behaves therefore as both a conductor and a capacitor. The W-element of the circuit denotes a Warburg capacitance described as $(i\,\omega\,\tau)^{1/2}$.

The cation exchange capacity reflects the number of exchangeable cations located on the surface of the mineral phase of the volcanic rock and is especially sensitive to the presence of clays and zeolites (Revil et al., 2002). The values of the mobility of ions in the diffuse layer is the same as in the bulk pore water with $\beta_{(+)}(\mathrm{Na}^+, 25\ ^\circ\mathrm{C}) = 5.2 \times 10^{-8}\ \mathrm{m^2\ s^{-1}\ V^{-1}}$. Finally, $\beta^S_{(+)}$ describes the mobility of the counterions in the Stern layer ($\beta^S_{(+)}(\mathrm{Na}^+, 25^\circ\mathrm{C}) = 1.9 \times 10^{-9}\ \mathrm{m^2\ s^{-1}\ V^{-1}}$, see Revil et al., 2017a; Revil et al., 2018).

Our model can be seen as a generalization of the Vinegar and Waxman (1984) model using an explicit dependence of the complex conductivity with the frequency and an origin of the polarization process occurring in the Stern layer of sorbed counterions on the mineral surface (Lyklema et al., 1983). This is what we call the dynamic Stern layer concept. The idea that the polarization can be associated with the cation exchange capacity of the porous medium can be traced back to Schufle (1959).

For completeness, and in the context of the dynamic Stern layer model, each time constant τ of the distribution $h(\tau)$ is associated with a pore size or grain size r (see discussions in Revil et al., 2010 and Revil, 2012) according to

$$\tau = \frac{r^2}{2D^S_{(+)}}, \tag{4}$$

where $D^S_{(+)}$ denotes the diffusion coefficient of the counterions in the Stern layer (expressed in $\mathrm{m^2\ s^{-1}}$). This diffusion coefficient is connected to the mobility of the counterions in the Stern layer, $\beta^S_{(+)}$, by the Nernst-Einstein relationship $D^S_{(+)} = k_b T \beta^S_{(+)}/|q_{(+)}|$, where T denotes the absolute temperature (in K), k_b denotes the Boltzmann constant ($1.3806 \times 10^{-23}\ \mathrm{m^2\ kg\ s^{-2}\ K^{-1}}$), and $|q_{(+)}|$ is the charge of the counterions in

the Stern layer coating the surface of the grains ($|q_{(+)}| = e$ where e is the elementary charge for Na^+). Therefore, according to Eq. (4), the probability density $h(\tau)$ can be transformed into a grain size (or pore size) probability density or (normalized) distribution, which would control in turn the transition between low and high frequencies in Eq. (1). For a broad distribution of polarization length scales, we can expect the complex conductivity to be characterized by a very broad distribution of relaxation times such that the phase may appear rather flat at least over a few orders of magnitude in frequency. We will come back to this point below (in terms of what is called Drake's model) since it calls for simplification of the equations.

The associated electrical circuit of a volcanic rock can be simplified to the model shown in Fig. 2. The in-phase conductivity can be written as

$$\sigma'(\omega) = \frac{1}{F}\sigma_w + \sigma_S(\omega), \tag{5}$$

where $\sigma_S(\omega)$ (in S m^{-1}) denotes a frequency dependent surface conductivity. This surface conductivity takes place in the electrical double layer coating the surface of the grains and comprises two contributions: one from the diffuse layer (frequency independent) and one from the Stern layer (which is frequency dependent). This surface conductivity has low-frequency and high-frequency asymptotic expressions given by (Fig. 2)

$$\sigma_S^0 = \left(\frac{1}{F\phi}\right)\rho_g\beta_{(+)}(1-f)\mathrm{CEC}, \tag{6}$$

$$\sigma_S^\infty = \left(\frac{1}{F\phi}\right)\rho_g B\,\mathrm{CEC}, \tag{7}$$

respectively (see also Niu et al., 2016a, 2016b) and where B is an apparent mobility defined by $B = \beta_{(+)}(1-f) + \beta^S_{(+)}f$. The normalized chargeability $M_n = M\sigma_\infty = \sigma_\infty - \sigma_0$, (in S m^{-1}) is proportional to the cation exchange capacity of the material according to

$$M_n = \left(\frac{1}{F\phi}\right)\rho_g\lambda\,\mathrm{CEC}, \tag{8}$$

and where $\lambda = \beta^S_{(+)}f$ is an equivalent surface mobility for the quadrature conductivity and the normalized chargeability (see Vinegar and Waxman, 1984). We note that the phase lag $\tan\varphi = \sigma''/\sigma'$ and the chargeability $M = M_n/\sigma_\infty$ (dimensionless) cannot be considered as true polarization parameters since they represent the ratio of a polarization parameter by a conduction parameter.

The introduction of a normalized chargeability with units in S m^{-1} may seem inappropriate to some research scientists since chargeability is already a normalized (dimensionless) quantity. The normalized chargeability was introduced in environmental geophysics to normalize the chargeability by the resistivity (pixel by pixel) in order to remove the fingerprint of resistivity on the inverted chargeability tomograms in absence of metallic particles (see Lesmes and Frye, 2001; Slater and Glaser, 2003; Mansoor and Slater, 2007). Indeed, M_n is proportional to the cation exchange capacity of the porous body while the chargeability and the conductivity depend strongly on the pore water salinity. In the presence of pyrite and magnetite, the chargeability remains the key parameters to plot since it is directly related to the volume content of metallic particles (Revil et al., 2015a, 2015b).

2.2. Influence of temperature

Since the present paper is dedicated to volcanic environments, it is important to study the effect of temperature on the complex conductivity. The temperature dependence of the conductivity depends on the temperature dependence of the mobility of the charge carriers, which in turn depend on the viscosity of the pore water. In this case, the use of an Arrhenius (semi-empirical) equation yields,

$$\sigma_w(T) = \sigma_o\,\exp\left(-\frac{E_a^w}{k_bNT}\right), \tag{9}$$

$$\sigma_w(T) = \sigma_w(T_0)\,\exp\left[-\frac{E_a^w}{k_bN}\left(\frac{1}{T}-\frac{1}{T_0}\right)\right], \tag{10}$$

where T and T_0 are expressed in degree Kelvin (K) ($T_0 = 298$ K, i.e., 25 °C), σ_o is a constant that has the dimension of a temperature independent conductivity, the product k_bN (product of the Boltzmann constant by the Avogadro number $N = 6.02 \times 10^{23}$ mol^{-1}) denotes the universal gas constant ($k_bN = 8.314$ J mol^{-1} K^{-1}), and E_a^w (expressed here in J mol^{-1}) denotes the activation energy associated with the viscosity of the pore water.

$$\lambda(T) = \lambda(T_0)\,\exp\left[-\frac{E_a^S}{k_bN}\left(\frac{1}{T}-\frac{1}{T_0}\right)\right], \tag{11}$$

$$B(T) = B(T_0)\,\exp\left[-\frac{E_a^S}{k_bN}\left(\frac{1}{T}-\frac{1}{T_0}\right)\right], \tag{12}$$

which corresponds to the temperature variations of $\beta_{(+)}$ (for Eq. (6)) and $\beta^S_{(+)}$ (for Eqs. (7) and (8)), respectively, $T_0 = 25$ °C (reference temperature), and E_a^S denote the activation energy for the viscosity of the bound water. Eqs. (11) to (12) implies that the surface conductivity, the normalized chargeability, and the quadrature conductivity depends on the temperature as

$$\sigma_S^\infty(T) = \sigma_S^\infty(T_0)\,\exp\left[-\frac{E_a^S}{k_bN}\left(\frac{1}{T}-\frac{1}{T_0}\right)\right], \tag{13}$$

$$M_n(T) = M_n(T_0)\,\exp\left[-\frac{E_a^S}{k_bN}\left(\frac{1}{T}-\frac{1}{T_0}\right)\right], \tag{14}$$

$$\sigma''(T) = \sigma''(T_0)\,\exp\left[-\frac{E_a^S}{k_bN}\left(\frac{1}{T}-\frac{1}{T_0}\right)\right]. \tag{15}$$

The chargeability of volcanic rocks M is expected to be temperature independent since it is a ratio of two quantities that have the same temperature dependence (Revil et al., 2017a, 2018).

2.3. Relationship between the normalized chargeability and the quadrature conductivity

According Revil et al. (2017a), the normalized chargeability M_n (determined between a low frequency and a high frequency) and the quadrature conductivity, σ'' (determined at the mean geometric frequency of the two frequencies used to define M_n) is given by

$$M_n = -\alpha\sigma'', \tag{16}$$

where the proportionality factor α is given explicitly by

$$\alpha \approx \frac{2}{\pi}\ln\,A, \tag{17}$$

and where $\ln(A)$ denotes the number of decades separating high and low frequencies. These equations can be derived in the context of the so-called constant phase model (i.e., the phase does not change too much with the frequency), also called the Drake's model (see Van Voorhis et al., 1973; Jonscher, 1981; Börner, 1992). Typically, α is in the range 5–10. Note that in Eq. (16) the quadrature conductivity is a negative quantity and the normalized chargeability is a positive quantity.

We can consider also the ratio between the high frequency surface conductivity and the quadrature conductivity

$$-\frac{\sigma''}{\sigma_S^\infty}=\frac{M_n}{\alpha\sigma_S^\infty}=\frac{\lambda}{\alpha B}. \tag{18}$$

In our previous works (e.g., Revil et al., 2017a, 2017b), we defined the dimensionless number R as the ratio of the normalized chargeability by the surface conductivity, i.e.,

$$\mathrm{R}\equiv\frac{M_n}{\sigma_S^\infty}\approx-\alpha\left(\frac{\sigma''}{\sigma_S^\infty}\right), \tag{19}$$

and therefore $-\sigma''/\sigma_S^\infty=\mathrm{R}/\alpha$. The dimensionless number $\mathrm{R}=\lambda/B$ can be related to the partition coefficient f and the mobility of the counterions in the Stern and diffuse layers

$$\mathrm{R}=\frac{\beta_{(+)}^S f}{\left[\beta_{(+)}(1-f)+\beta_{(+)}^S f\right]}. \tag{20}$$

This dimensionless parameter is of paramount importance to go from the polarization parameters (M_n or σ'') to the surface conductivity.

2.4. Influence of metallic particles

Volcanic areas can host sulfide deposits (Ohmoto, 1996) and basaltic rocks can contain significant amounts of magnetite. Metallic particles can also exert a very strong influence on the complex conductivity of porous rocks (e.g., Van Voorhis et al., 1973). For volcanic rocks, a volume content of pyrite, magnetite or other metals and semi-metals (in a broad sense) higher than 0.3% can have a significant impact on the chargeability and phase (see discussions in Revil et al., 2015a, 2015b). The chargeability M entering Eq. (1) is directly related to the (dimensionless) volume content of metallic particles φ_m (Revil et al., 2015a, their Equations 69 and 70),

$$M\approx 1-\left(1-\frac{9}{2}\varphi_m\right)(1-M_b), \tag{21}$$

$$M\approx\frac{9}{2}\varphi_m+M_b. \tag{22}$$

In Eq. (22), M_b (dimensionless) denotes the chargeability of the background volcanic rock material given by

$$M_b=\left(\frac{1}{F\phi}\right)\frac{\rho_g\lambda\,\mathrm{CEC}}{\sigma_b^\infty}, \tag{23}$$

where σ_b^∞ denotes the instantaneous conductivity of the background rock material. It is given by

$$\sigma_b^\infty=\frac{1}{F}\sigma_w+\left(\frac{1}{F\phi}\right)\rho_g B\,\mathrm{CEC}, \tag{24}$$

Therefore the background chargeability is given by

$$M_b=\frac{\rho_g\lambda\,\mathrm{CEC}}{\phi\sigma_w+\rho_g B\,\mathrm{CEC}}, \tag{25}$$

Interestingly, at low salinitie (i.e., for freshwater-saturated volcanic rocks), the background chargeability is given by a constant value equal to R.

$$\lim_{\sigma_w\ll\sigma_S} M_b=\frac{\lambda}{B}=R, \tag{26}$$

Therefore at low salinities, we have

$$M=\frac{9}{2}\varphi_m+R. \tag{27}$$

We will test this equation in this paper in order to test the influence of pyrite on the chargeability of pyrite-rich volcanic rocks.

3. Origin of the core samples

3.1. Merapi and Papadayan volcanoes, Indonesia

The lavas from Papandayan (Fig. 3) are mainly basaltic andesite, pyroxene andesite, and pyroxene dacite (Asmoro et al., 1989). The Papandayan samples contain pyroclasts with clinopyroxene crystals with simple core-rim zoning (typically ~ 5–15 vol%), euhedral magnetite crystals, unresorbed amphiboles, and iron oxides. Petrological studies on Papandayan lavas show that the most abundant alteration minerals in the altered materials are polymorphs of silica, pyrite, pyrophyllite, natroalunite, and kaolinite (Mazot, 2005).

Merapi (Fig. 4) is an almost persistently active basaltic to basaltic andesite volcanic complex in Central Java (Indonesia) (e.g., Voight et al., 2000; Surono Jousset et al., 2012) and often referred to as the type volcano for small-volume pyroclastic flows generated by gravitational lava dome failures. The lavas of Merapi are typically basaltic andesites with a porphyritic texture consisting of a glassy groundmass with abundant microlites that hosts phenocrysts of plagioclase, clinopyroxene, amphibole, and Fe-Ti oxides (Erdmann et al., 2014, 2016; Kushnir et al., 2016). Altered dome materials, light grey in color, are cristobalite-rich and contain diktytaxitic textures (Kushnir et al., 2016).

Our laboratory measurements were performed on 16 consolidated cubic samples and 16 unconsolidated samples (see Tables 1 and 2). The average length and width of the cubic samples is 5 and 2.5 cm, respectively (Fig. 5). These samples were extracted from larger cores sampled on the outcropping formations of these two volcanoes.

3.2. Furnas volcano, Azores, Portugal

The second set of samples is 5 unconsolidated volcanic rocks from Furnas trachytic volcano in Portugal (Table 3 and Fig. 6) that must belong to the last explosive eruptions that occurred in this volcanic system. Furnas volcano is a central volcano located in the Eastern side of São Miguel Island, in the Azores volcanic archipelago. Furnas volcano comprises an impressive summit depression 5 × 8 km wide formed by two nested calderas (Guest et al., 1999, 2015) and volcanic products up to 100,000 years BP old (see Moore, 1990). Furnas volcanic activity has been characterized by several eruptive styles, ranging from mid-effusive activity to caldera-forming explosive events (Guest et al., 1999, 2015). Ten intracaldera moderately explosive trachytic eruptions occurred in this volcano in the last 5000 years, two of which occurred in historical times (1439–43; 1630) (Guest et al., 2015). These historical subplinian/phreatomagmatic eruptions formed two tuff and pumice rings with central trachytic domes and its deposits mantle the caldera floor. The collected samples represent this type of material. Nowadays, volcanic activity at Furnas volcano is characterized by secondary manifestations of volcanism, which comprises low temperature fumaroles (95 to 100 °C), steaming ground, thermal and cold CO_2-rich springs, as well as soil diffuse outgassing areas (e.g., Viveiros et al., 2010; Silva et al., 2015). The caldera of Furnas volcano also contains several monogenetic trachytic domes in addition to the historical ones. A recent study carried out by Jeffery et al. (2016) indicates that Furnas trachytes are mainly derived from fractional crystallisation of alkali basalt parental magmas, at depths between approximately 3 and 4 km.

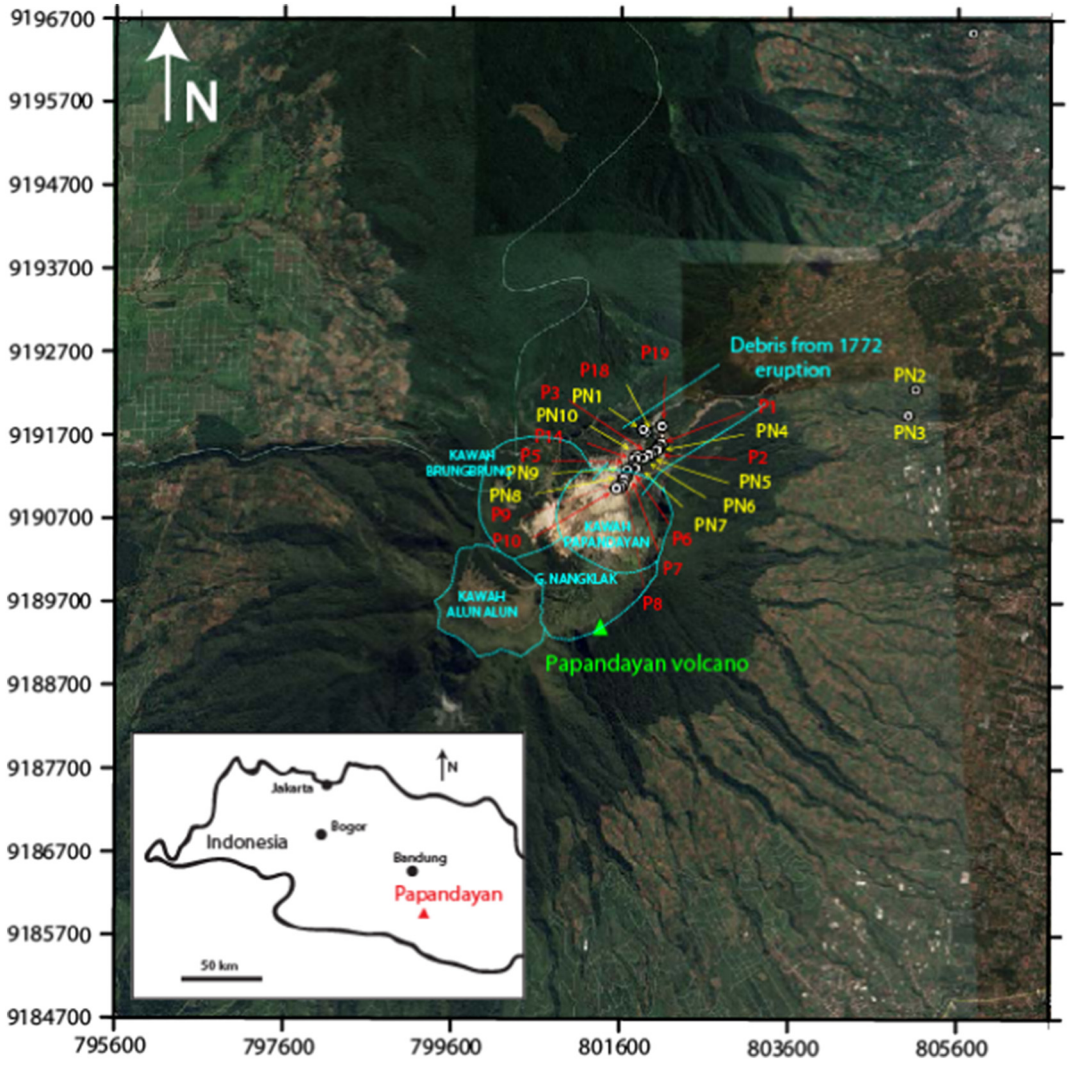

Fig. 3. Papandayan volcano, Indonesia. The samples were extracted from the area around Kawah Baru (literally "new crater") that was formed during the last 2002 phreatic eruption. This figure shows the position of the samples with their code names (coordinate system, UTM WGS84, 48M). The inset shows a map of the Western part of Java Island (Indonesia) with the position of Papadayan volcano (red triangle). (For interpretation of the references to color in this figure legend, the reader is referred to the web version of this article.)

3.3. Yellowstone Caldera, USA

The next set of volcanic rock samples consists of 26 samples collected at Yellowstone National Park (USA, Fig. 7). The first subset comes from the ground surface in the Solfatara Plateau Thermal Area (SPTA), which corresponds to an acid-sulfate vapor-dominated area near the northern rim of the 0.63 Ma Yellowstone Caldera (16YS series in Table 3, Fig. 8). An additional set of samples is from drill hole Y-2 (drilled to a depth of 157 m) in Yellowstone's Lower Geyser Basin and drill hole Y-8 in the Upper Geyser Basin (Y2 and Y8 series Table 3). Samples of the 16YS series consist of acid-sulfate altered glacial deposits which, in turn, consist mainly of fragments from the 110 ± 3 ka Solfatara Plateau flow rhyolite (Christiansen, 2001) with various levels of alteration. Detailed descriptions of alteration mineralogy from drill hole Y-2 can be found in Bargar and Beeson (1981) and for Y-8 in Keith et al. (1978). The chemical composition of the core from both drill holes is provided in Beeson and Bargar (1984). The samples we used have a cylindrical shape with a diameter of 2.5 cm and a length of 2 cm. The cylinder plugs were obtained by drilling perpendicular to the main core axis (Fig. 8). The samples are from rhyolite flows and breccia. Core from drill hole Y-2 consists of interbedded glacial sediments interlayered with pumiceous tuff from 10 to 32 m, and rhyolitic of the 0.153 ± 0.002 Ma Elephant Back rhyolite flow (Christiansen, 2001) and the 0.151 ± 0.004 Mallard Lake rhyolite flow from 32 to 157 m (Bargar and Beeson, 1981) (Fig. 8). Pervasive hydrothermal alteration of the rhyolite is nearly continuous throughout the drill core. Core from drill hole Y-8 consists of 54 m of glacial sediments, 8 m of rhyolite flow breccia, and 91 m of pumiceous tuff.

3.4. Whakaari volcano (White Island), New Zealand

The last set of samples was sourced from Whakaari volcano (White Island), an active andesitic-dacitic stratovolcano located at the north-eastern end of the Taupō Volcanic Zone, New Zealand (Fig. 9). The 22 core samples are shown in Fig. 10. The volcano hosts a hydrothermal system (Giggenbach et al., 2003) that is expressed at the surface as hot springs, bubbling mud pools, sulphur-encrusted fumaroles and chimneys, and acid streams and pools. The result of this hydrothermal activity is that a large proportion of the rocks forming the crater floor and walls are hydrothermally altered (Hedenquist et al., 1993; Moon et al., 2005; Heap et al., 2015, 2017). Although Strombolian activity occurred during the late seventies and mid-eighties (Houghton and Nairn, 1991), volcanic activity at Whakaari is characterized by phreatic and phreatomagmatic eruptions (Mayer et al., 2015).

The present-day crater walls chiefly comprise interbedded lavas, lava breccias, and tuffs with a dominantly ash-sized particle size ("ash tuffs")

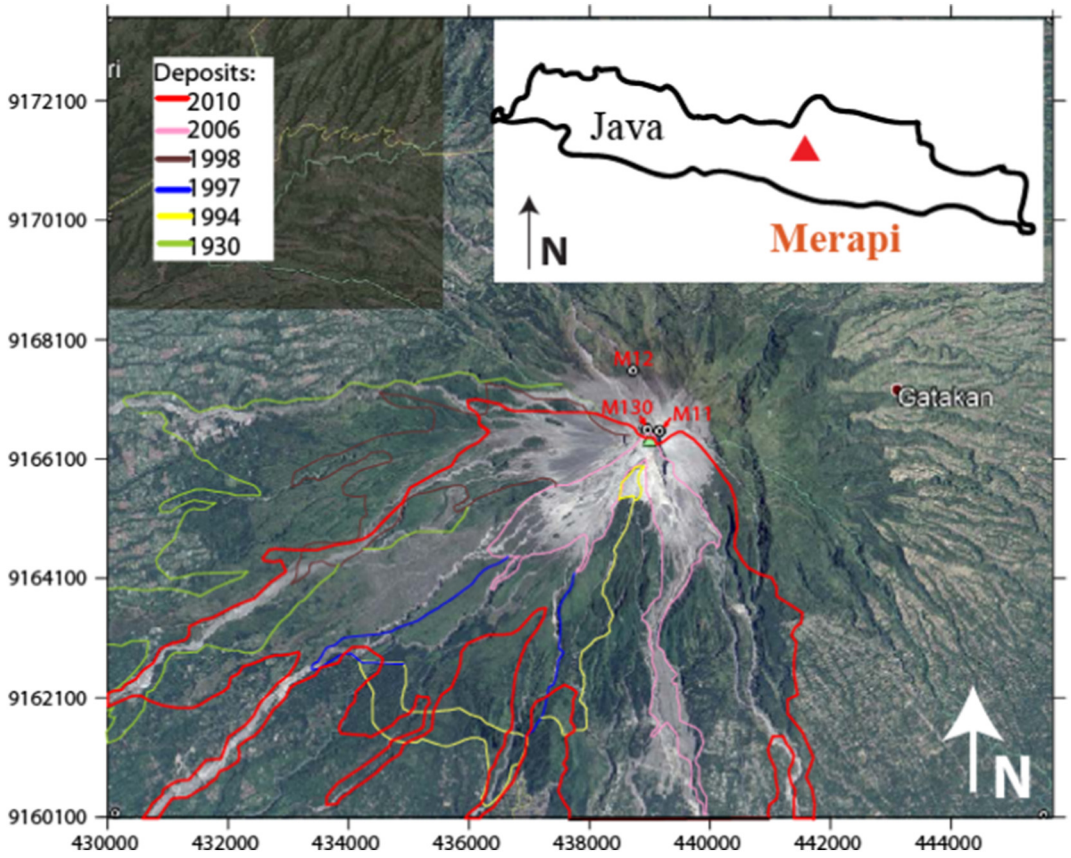

Fig. 4. Merapi volcano, Java Island (Indonesia), with the position of the three core samples on this stratovolcano (coordinate system, UTM WGS84, 49M). The inset shows a map of the Java Island (Indonesia) with the position of Merapi volcano (red triangle). (For interpretation of the references to color in this figure legend, the reader is referred to the web version of this article.)

(Heap et al., 2017). Blocks of these representative rock types were collected at the sampling sites shown in Fig. 9 and cylindrical cores (2 cm in diameter and 4 cm in length) were prepared for laboratory analyses (Fig. 10). The permeability of these samples, measured for another publication (Heap et al., 2017), is provided in Table 5. The lava is andesitic and contains phenocrysts and microlites of feldspar and pyroxene within a groundmass of hydrated amorphous glass. The lava contains precipitated jarosite and gypsum within pores and microcracks and cristobalite (Heap et al., 2017). The lava breccia chiefly comprises angular lava fragments (containing amorphous silica, plagioclase, and pyroxene). The lava breccia also contains cristobalite and kaolinite (Heap et al., 2017). The ash tuff samples are composed of partially cemented ash-sized crystal and opalised glass (now hydrated amorphous silica) fragments. The ash tuff samples can be subdivided into two groups: those that are white in color and contain alunite and those grey in color that do not. More information on these materials can be found in Heap et al. (2015, 2017).

Table 1
Relevant petrophysical of the 16 core samples from Merapi and Papandayan volcanos in Indonesia. The quantity ρ_g denotes the grain density (kg m^{-3}), ϕ the connected porosity (dimensionless), F the electrical (intrinsic) formation factor (dimensionless), CEC (expressed in meq/100 g) denotes the cation exchange capacity, and σ'' (in Sm^{-1}) denotes the quadrature conductivity at 1 Hz.

Sample	ϕ (−)	ρ_g (kg m^{-3})	F (−)	CEC (meq/100 g)	σ_S (10^{-4} S m^{-1})	σ'' (10^{-5} S m^{-1})
M11a	0.132	2595	51	0.611	1.5	0.7
M11b	0.171	2739	30	0.550	1.2	0.4
M12	0.205	2947	23	0.691	–	1.7
M130	0.143	2842	48	0.527	1.5	1.1
P1	0.022	2759	4334	1.181	15.3	0.8
P2	0.031	2551	7540	4.661	7.1	0.8
P3	0.033	2707	2335	4.512	18.7	5.7
P5	0.038	2681	2051	3.428	15.8	2.0
P6	0.044	2700	1573	1.626	8.0	1.2
P7	0.030	2789	5132	1.290	24.8	0.5
P8	0.032	2706	984	4.482	17.4	2.0
P9	0.037	2863	2337	1.566	13.9	2.2
P10	0.037	2684	1308	1.590	30.4	13.7
P14	0.057	2737	387	1.311	11.7	1.0
P18	0.056	2824	686	1.309	33.7	1.7
P19	0.030	2815	4173	–	21.0	2.1

4. Experiments

4.1. Induced polarization experiments

We use a four electrodes technique to perform the complex conductivity measurements, i.e., we separate the current electrodes A and B from the voltage electrodes M and N (which is a classical notation in geophysics, see for instance Herman, 2001; Michot et al., 2016). The complex conductivity measurement was conducted with a high-precision impedance analyzer (Zimmermann et al., 2008) (Fig. 11a). Two different sample holders are used for the consolidated and unconsolidated samples, the same setup used by Revil et al. (2018). For the consolidated samples (cubic and core samples), the current electrodes are self-adhesive superconductive carbon film electrodes with biocompatible hydrogel commonly used in general and neonatal cardiology with the same size as the sample. We use an insulating tape around the external side of the samples to avoid the drying of the sample during the measurements (Fig. 11b). Two current electrodes (A and B) are placed at the end faces as current electrodes and two other electrodes are used on the side of the cylindrical cores as voltage electrodes (M and N). A

Table 2
Relevant petrophysical of the 16 unconsolidated samples from Merapi and Papandayan volcanoes in Indonesia. The quantity ρ_g denotes the grain density (kg m^{-3}), ϕ the connected porosity (dimensionless), F the electrical (intrinsic) formation factor (dimensionless), CEC (expressed in meq/100 g) denotes the cation exchange capacity, σ'' (in Sm^{-1}) denotes the quadrature conductivity at 1 Hz and pore water conductivity 0.17 Sm^{-1} (NaCl), and S_{sp} corresponds to the specific surface area measured with the BET technique.

Sample	ϕ (−)	ρ_g (kg m^{-3})	F (−)	CEC (meq/100 g)	S_{sp} (m^2/g)	σ_S (10^{-4} S m^{-1})	σ'' (10^{-5} S m^{-1})
MER M01 Bandit	0.396	2389	6	0.600	0.69	–	2.1
MER NF1	0.462	3218	5	0.200	1.87	17.8	4.2
MER NF2	0.525	3578	4	0.200	1.12	–	3.0
MER SV6	0.473	2661	5	0.300	0.29	8.8	2.7
MER T3	0.414	2621	7	0.300	2.13	5.5	2.6
MER Turist	0.388	2470	6	2.475	5.15	2.6	15.3
PN 1	0.715	2270	5	12.112	45.28	99.8	59.3
PN 2	0.653	2168	4	25.930	33.30	336.5	127.1
PN 3	0.707	2679	5	19.749	102.75	318.1	121.7
PN 4	0.634	3042	6	6.881	34.66	42.1	21.0
PN 5 SN1	0.566	1693	6	33.895	5.40	–	10.4
PN 6	0.722	3143	5	28.396	7.43	328.2	49.8
PN 7	0.648	2473	5	11.385	29.43	392.6	59.8
PN 8	0.686	2294	5	11.580	51.32	252.8	40.8
PN 9	0.578	2017	4	3.560	25.65	210.4	22.4
PN 10	0.625	2771	8	5.719	21.63	100.5	19.3

spring was used to push the current electrodes against the sample to maintain a constant uniaxial stress.

For unconsolidated samples, we keep the samples in their water-filled buckets with a cap to avoid drying during the course of the experiments. Four equally spaced non-polarizing Ag-AgCl sintered electrodes (diameter 4 mm) are placed in the top of the sample holder with the cap (Fig. 11c). The interval between two consecutive electrodes is 2 cm, and the height and diameter of the bucket is 2.5 and 7 cm, respectively (Fig. 11c). The measured resistances were transformed to resistivity using a geometrical factor numerically computed based on the geometry of the sample and the position and size of the electrodes.

The rock samples were initially saturated with a low salinity NaCl solution in a vacuum chamber for 24 h. Then samples were left at least two weeks in the solution in a closed container, and fluid conductivity was

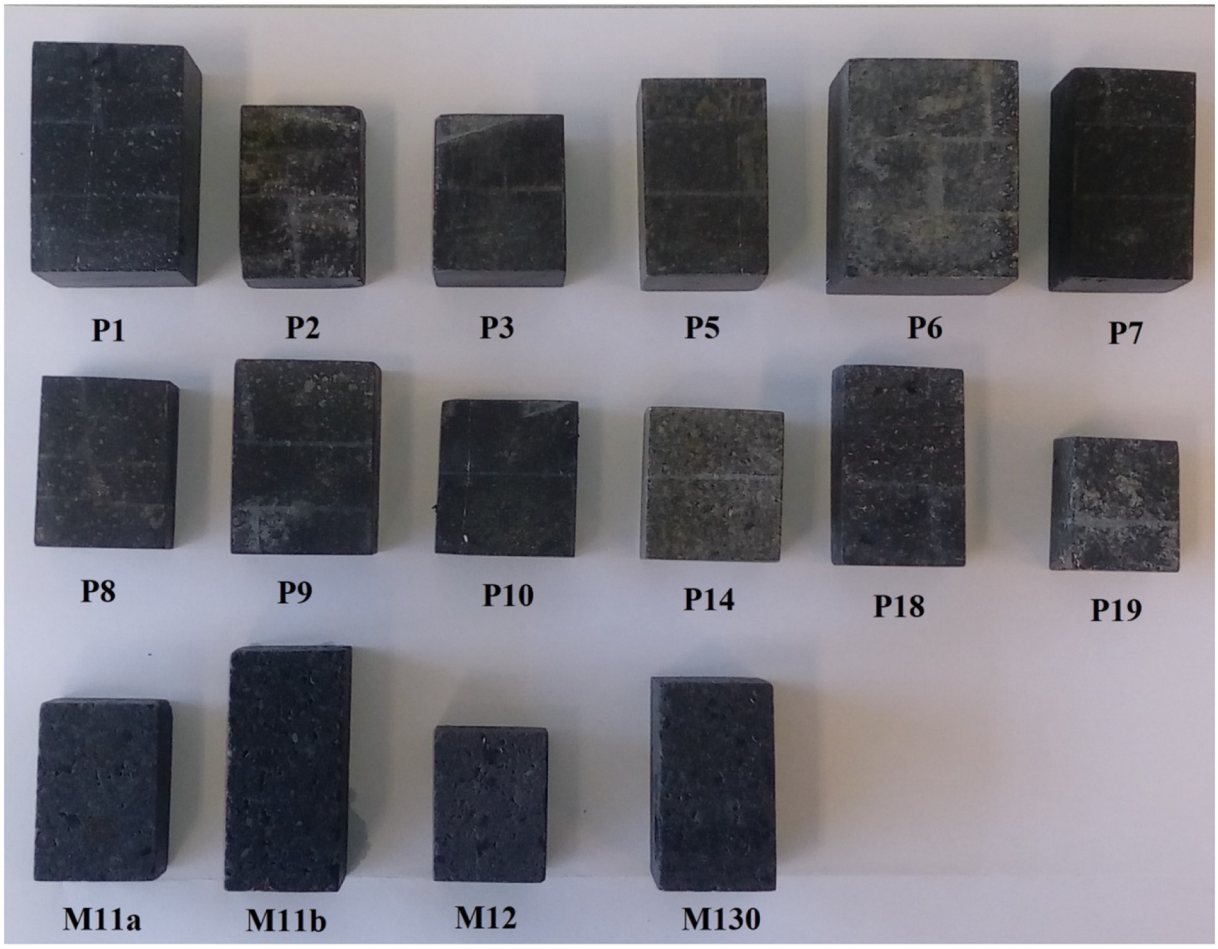

Fig. 5. Picture of the 16 consolidated core samples from Papandayan and Merapi volcanoes (Indonesia). These samples are relatively low porosity core samples.

Table 3
Relevant petrophysical of the 5 core samples from Furnas volcano in the Azores (Portugal). The quantity ρ_g denotes the grain density (kg m^{-3}), ϕ the connected porosity (dimensionless), F the electrical (intrinsic) formation factor (dimensionless), CEC (expressed in meq/100 g) denotes the cation exchange capacity, and σ'' (in Sm^{-1}) denotes the quadrature conductivity at 1 Hz.

Sample	ϕ (−)	ρ_g (kg m^{-3})	F (−)	CEC (meq/100 g)	S_{sp} (m^2/g)	σ_S (10^{-4} S m^{-1})	σ'' (10^{-5} S m^{-1})
FUR 1	0.552	2376	8	4.246	5.79	18.5	13.6
FUR 2	0.671	3441	4	0.600	0.46	13.4	7.2
FUR 5	0.630	3559	5	0.900	2.94	31.2	2.8
FUR 7	0.651	3288	4	0.200	0.47	192.7	6.8
FUR SP	0.701	1589	2	2.894	34.14	269.0	9.9

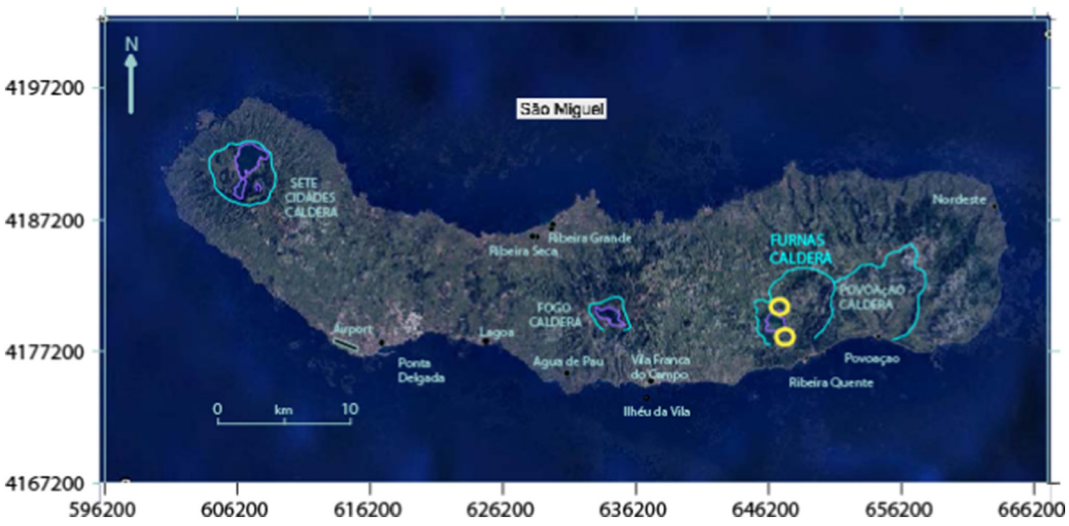

Fig. 6. Furnas caldera, Azores (Portugal) in the Atlantic Ocean. The samples were collected at the northern portion of the lake and on 1630 dome. The two yellow circles indicate the position of the areas where the samples were taken. (coordinate system, UTM WGS84, 26S). (For interpretation of the references to color in this figure legend, the reader is referred to the web version of this article.)

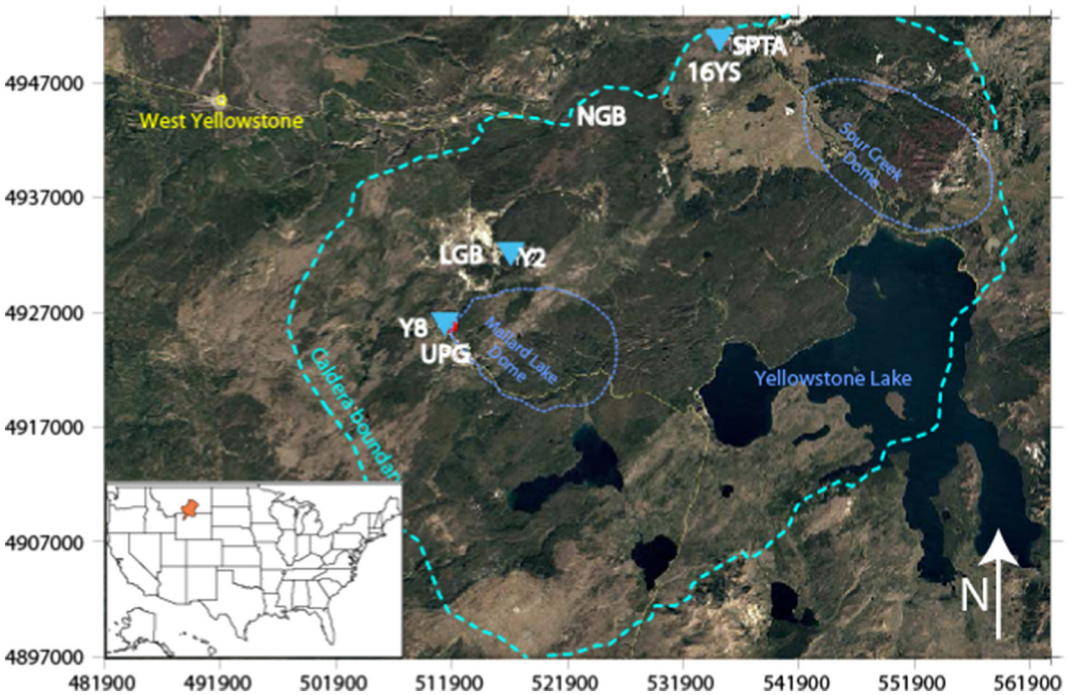

Fig. 7. Yellowstone with the location of the rock samples collected in the field (blue triangles). Three families of core samples have been collected in borehole Y-2 (interbedded glacial sediments interlayered with pumiceous tuff and rhyolitic), borehole Y-8 (glacial sediments, rhyolite flow breccia, and pumiceous tuff), and borehole 16-YS (acid-sulfate altered glacial deposits). The inset shows a map of the United States with the position of the Yellowstone caldera (red area). Coordinate system, UTM WGS84, 12T. SPTA: Solfatara Plateau Thermal Area, NGB: Norris Geyser Basin, UPG: Upper Geyser Basin, LGB: Lower Geyser Basin. Dotted lines: limit of the caldera. (For interpretation of the references to color in this figure legend, the reader is referred to the web version of this article.)

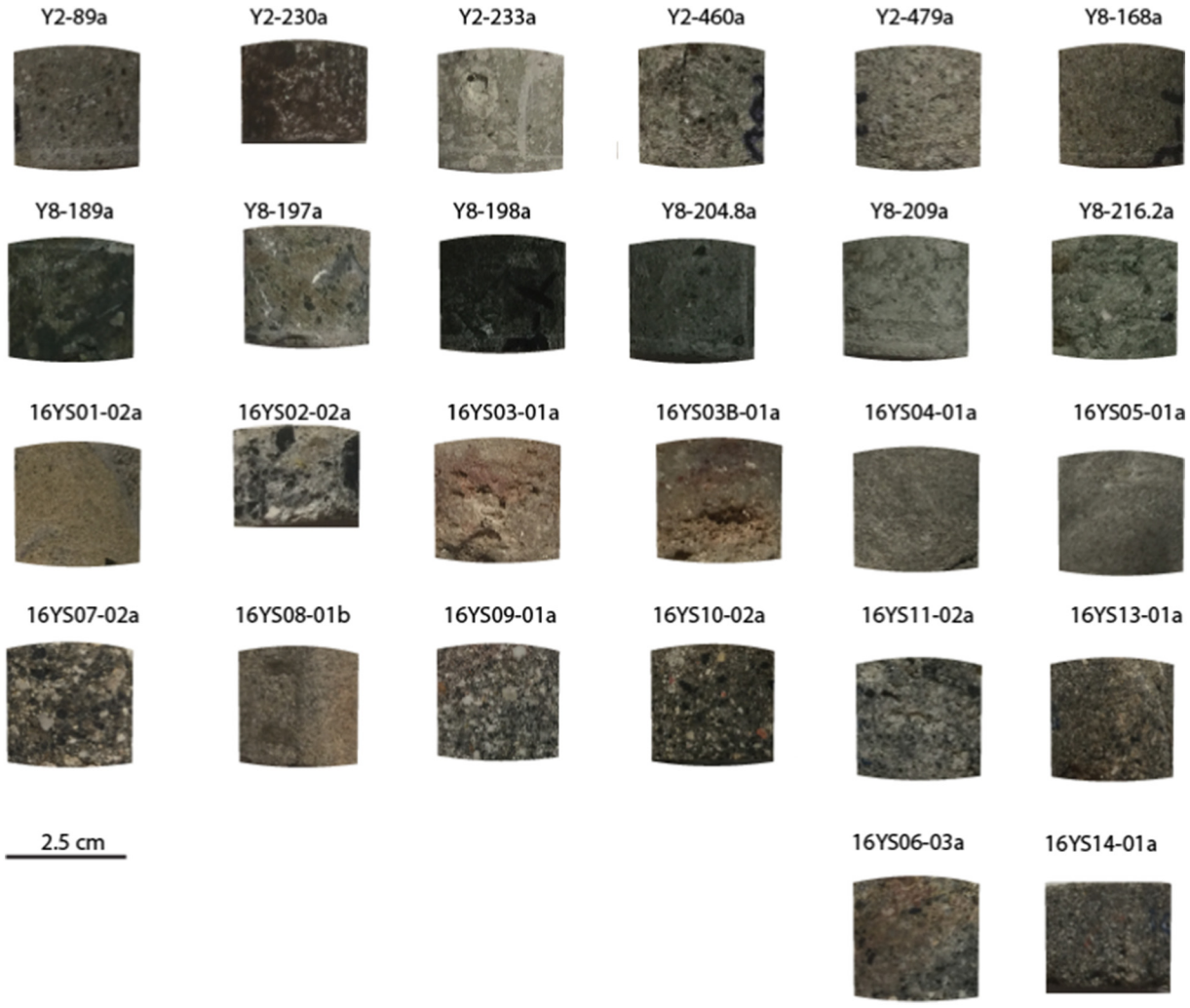

Fig. 8. Picture of the 28 core samples from Yellowstone Park (USA).

measured until the value stabilized. Afterwards, the samples were removed from their containers for complex conductivity measurements using a frequency from 10 mHz to 45 kHz. Complex conductivity spectra were obtained at pore fluid conductivities 0.01, 0.1, 1.0, and 10 S m^{-1} for the consolidated samples and at pore fluid conductivities 0.1, 1.0, and 10 S m^{-1} for the unconsolidated samples. Data with positive phases and/or standard deviations in excess of 10% were not considered in our analysis. The fluid conductivity σ_w and temperature T of the NaCl solutions were also measured using a calibrated conductivity meter. The same procedure was repeated to obtain the complex conductivity of each sample at all the pore fluid conductivities. For each conductivity, the solution in which the samples were immersed was changed to enforce the value of the desired conductivity. Equilibrium was reached following several weeks. Examples of complex conductivity spectra (real and imaginary parts versus frequency) are shown in Fig. 12. Changes in both the in-phase and the quadrature conductivities with salinity are small when pore water conductivity is small (0.01 and 0.1 S m^{-1} in comparison higher pore water salinities 1 and 10 S m^{-1}).

We also performed a set of measurements in which we mix some pyrite grains (typical grain size of 1 cm, grain density 5250 kg m^{-3}) with a crushed volcanic rock (MERTurist) at 0.17 S m^{-1} (NaCl, 25 °C). This was done to investigate the effect of the volumetric pyrite content on the chargeability. The total sample volume in these experiments was 77.8 cm^3.

4.2. Other petrophysical measurements

In addition to the complex conductivity spectra, we measured some petrophysical properties of the 85 rock consolidated and unconsolidated volcanic samples (reported in Tables 1 to 5). The (connected) porosity and density of the mineral phase were determined using the volume and mass of the dry and saturated samples. The Cation Exchange Capacity (CEC) measurements were obtained using the cobalt hexamine chloride method (Ciesielski and Sterckemann, 1997 and Aran et al., 2008). Because of sorption of the cobalt on the surface of the clay minerals and zeolites, the color of the solution becomes weaker. CEC and concentration of exchangeable clay cations are calculated based in the absorbance measurements with a calibrated spectrophotometer at 472 nm. The CEC values provided in Tables 1 to 5 are expressed in meq/100 g (which is the traditional unit for this parameter) and can be converted in the international system of units using 1 meq/100 g = 963.20 C kg^{-1}. In our experiments, the pH of the solutions was not buffered and some rocks were acidic while others were basic.

The specific surface area of some of the core samples was determined using the BET nitrogen adsorption technique using a nitrogen sorption isotherm. The underlying theory of the BET nitrogen sorption approach can be found in Brunauer et al. (1938). The method is used to determine the specific surface area (in m^2 g^{-1}) of the rock samples. The samples were degassed at 80 °C. Tables 2 and 5 show the specific

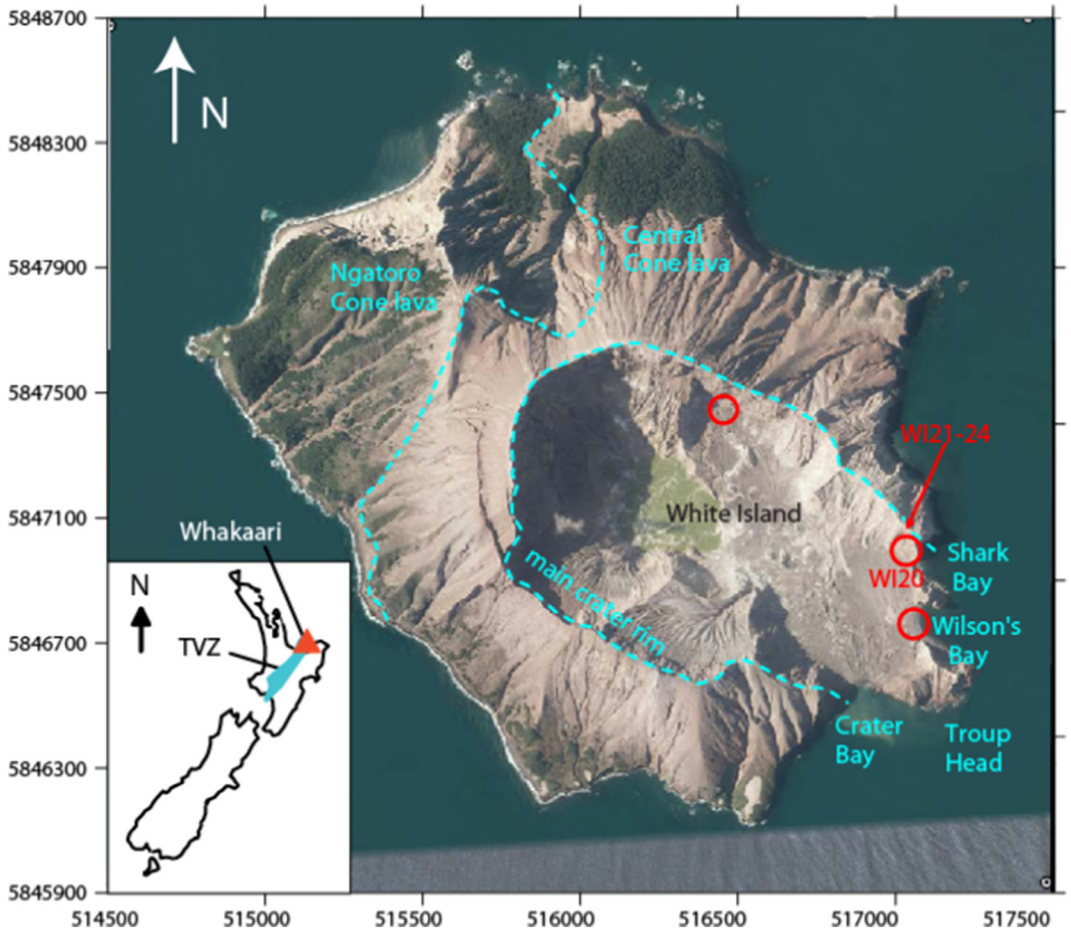

Fig. 9. Map of Whakaari/White Island volcano (Bay of Plenty, New Zealand) showing the locations of the sample collection sites (indicated by the red open circles). The inset shows a map of New Zealand showing the location of the Taupō Volcanic Zone (TVZ, blue area) and Whakaari volcano (red triangle). Figure modified from Heap et al. (2017) (coordinate system, UTM WGS84, 60M). (For interpretation of the references to color in this figure legend, the reader is referred to the web version of this article.)

surface area determined for unconsolidated samples Merapi and Papandayan and the core samples from Whakaari volcano. The ratio of the CEC to the specific surface area defines the mean surface charge density Q_s of the minerals (typically 1 to 5 elementary charges per nm^2). For sedimentary rocks, the surface charge density depends on the pH of the pore water and usually the CEC is reported at near neutral pH conditions (pH = 7).

5. Results

5.1. Specific surface area versus cation exchange capacity

Fig. 13 shows the specific surface area data as a function of the cation exchange capacity for the volcanic rocks investigated in the present study. Fig. 13 also includes data from volcanic rocks from Hawaii and tight sandstones from Revil et al. (2018). For volcanic rocks, it is known that specific surface area measurements can be used as a proxy of alteration (see Nielsen and Fisk, 2008). The pertinent question is whether the CEC can also be considered as a proxy of alteration.

In our study, the two quantities are proportional to each other with an average surface charge density ($Q_s = 0.90$ C m^{-2}, ratio of the CEC to the specific surface area) equivalent to 6 elementary charges per nm^2. This value is consistent with what is found in sedimentary rocks (Revil, 2013) and basaltic rocks (Revil et al., 2017a). Since the equilibrium pH of the pore waters used to determine the CEC was different for different families of core samples, we propose that the CEC can be used as a proxy of alteration. Such a statement would probably deserve, however, a future study.

5.2. Formation factor and surface conductivity

The conductivity of each sample (measured at 1 Hz) is plotted as a function of the pore water conductivity in Fig. 14 for three core samples. The data are then fitted with Eq. (5) in order to determine the intrinsic formation factor F and the surface conductivity σ_S. In our study, the formation factors ranges from 2.5 for the very porous unconsolidated cores to 7540 for a low-porosity core sample. The surface conductivity ranges from 10^{-4} to 4×10^{-2} S m^{-1} (see Tables 1 to 5).

Fig. 15 shows the (intrinsic) formation factor data versus the connected porosity of the 85 volcanic samples used in this study. We also plot published data for volcanic rocks from Hawaii in Fig. 15 (from Revil et al., 2017b). The datasets exhibit at first approximation a power law relationship and can be fitted with Archie's law (Archie, 1942). The fit with Archie's law yields an average cementation exponent $m = 2.31$ ($R^2 = 0.74$), which is more than the cementation exponent recorded for sedimentary rocks ($m = 2$). It is due to the more complex nature of the connected pore space in volcanic materials (see, for example, Shea et al., 2010; Heap et al., 2014; Farquharson et al., 2015; Colombier et al., 2017).

In Fig. 16, we compare the surface conductivity versus the CEC (corrected for the tortuosity of the bulk pore space $F\phi$) for volcanic and sedimentary rocks. The rational for plotting the surface conductivity versus the ratio CEC/$F\phi$ is dictated by Eqs. (6) and (7). The linear trend observed in this figure is consistent with previous studies (e.g., Revil et al., 2017a, 2017b). This trend reflects the effect of the alteration of the volcanic rocks on their surface conductivity. Using the value of the slope $a = \rho_g B$ and using $\rho_g = 3000$ kg m^{-3}, we

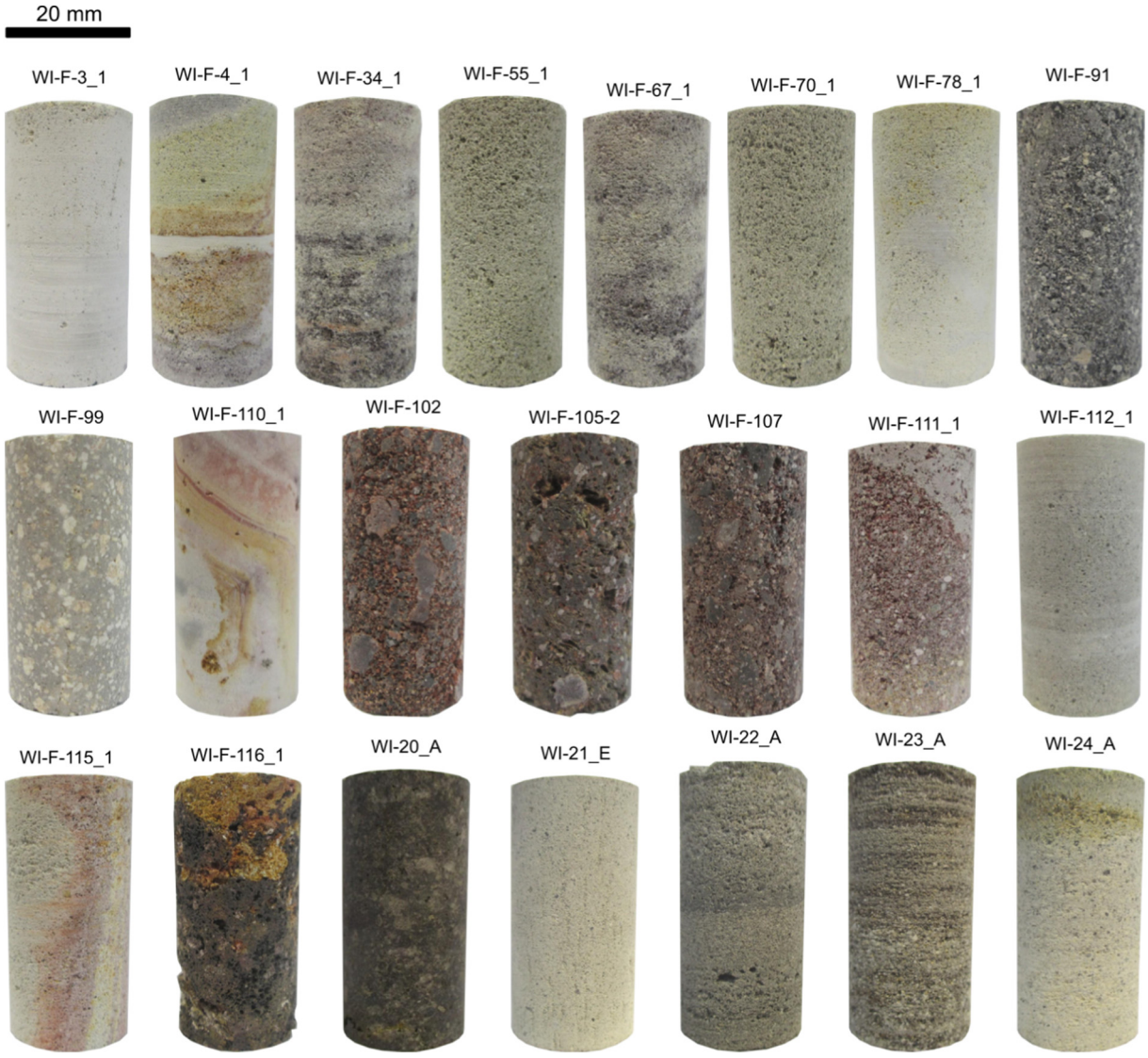

Fig. 10. Pictures of the 22 core samples from Whakaari/White Island volcano (Bay of Plenty, New Zealand) showing their textures and sample-scale laminations.

obtain $B(Na^+, 25\ °C) = 4.1 \times 10^{-9}\ m^{-2}\ s^{-1}\ V^{-1}$. This value is consistent with the value obtained in Revil et al. (2017a) for basaltic rocks ($B(Na^+, 25\ °C) = 4.3 \times 10^{-9}\ m^{-2}\ s^{-1}\ V^{-1}$).

5.3. Quadrature conductivity

In Fig. 17, the quadrature conductivity is plotted as a function of the normalized CEC (the CEC divided by the tortuosity $F\,\phi$ of the bulk pore space). We observe again a linear trend, i.e. the quadrature conductivity is controlled by the degree of alteration of the volcanic rocks.

In Fig. 18, we plot the magnitude of the quadrature conductivity versus the surface conductivity. As predicted from the theory, the quadrature conductivity and surface conductivity are proportional to each other (see Eq. (18)). The linear corresponds to $-\sigma''/\sigma_S^\infty = 0.022$ (correlation coefficient $R^2 = 0.67$) is obtained for the volcanic rocks used in this study. Since we have $-\sigma''/\sigma_S^\infty = R/\alpha$ and $\alpha = 4.06$ (Fig. 19), this yields $R = 0.089$ ($R = 0.12$ if we directly correlate the normalized chargeability to the surface conductivity, see Fig. 20). In all these equations, note that the quadrature conductivity is a negative quantity. That said, if we take $\alpha = 10$ (i.e., using the very high and low frequencies to determine the normalized chargeability), we obtain $R = 0.22$. These ratios agree fairly well with the data obtained in the last decade for sedimentary rocks (see Revil et al., 2018 and references therein). Revil et al. (2017a) obtained $R = 0.37$ for basaltic rocks (using a normalized chargeability determined on a broader frequency range) while Revil et al. (2018) obtained $-\sigma''/\sigma_S = 0.037$ (compare with $-\sigma''/\sigma_S^\infty = 0.022$ in the present study) for soils at higher pore water conductivity (0.5 to 1 Sm^{-1}).

5.4. Normalized chargeability

Fig. 19 shows the relationship between the normalized chargeability ($M_n = \sigma_\infty$-σ_0, in $S\ m^{-1}$) and the quadrature conductivity. Such relationship is important to connect the induced polarization usually performed in field conditions in the time-domain (and measuring the chargeability) to the frequency-domain induced polarization data such as those presented in this paper. We will come back to this point in the last section of the manuscript.

Normalized chargeability can be determined from the amplitude of the in-phase conductivity at low frequency and high frequency asymptotic values. In this study, we estimated the normalized chargeability from in-phase conductivities at frequencies of 1 Hz and 1 kHz. Normalized chargeability can be estimated during the time domain induced polarization investigation in a laboratory and field measurements from chargeability M, as $M_n = M\,\sigma_\infty$.

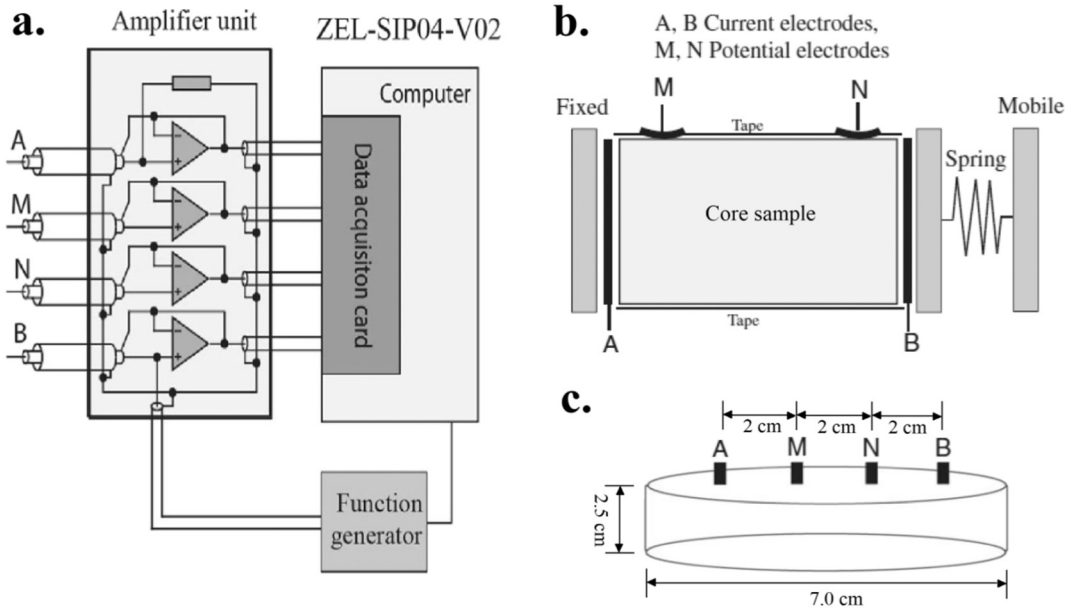

Fig. 11. Impedance meter, sample holders and position of the A–B current electrodes and M-N measured voltage electrodes on the surface of the samples. a. ZEL-SIP04-V02 impedance meter (Zimmermann et al., 2008) used for the laboratory experiments. b. Sample holder used for rock cubic and core samples (consolidated samples). The electrodes are self-adhesive superconductive carbon film electrodes with biocompatible hydrogel commonly used in general and neonatal cardiology (see Revil et al., 2018). c. Sample holder used for unconsolidated volcanic core samples. Ag/AgCl sintered electrode for the A, B, M, and N electrodes. The geometrical factor is computed from numerical modeling using Comsol Multiphysics (see Revil et al., 2018).

Revil et al. (2017a) supposed that the phase lag $\tan\varphi = \sigma''/\sigma'$ is not frequency dependent on studied spectra (Drake's model). Phase lag $\varphi(\omega)$ is measured during spectral induced polarization investigations when a sinusoidal current is injected. It is the phase lag between injected sinusoidal current and measured potential sinusoidal signal. They supposed a turning frequency point where σ_0 change to σ_∞ on the in-phase conductivity spectra at the geometric mean frequency. The geometric is a mean frequency between a low frequency for which the conductivity is close to σ_0 and a high frequency for which the conductivity is close to σ_∞.

The normalized chargeability between 1 Hz and 1 kHz and the quadrature conductivity determined at the geometric mean frequency of 32 Hz are plotted in Fig. 19. This normalized chargeability is defined as the difference in the in-phase conductivity between 1 kHz and 1 Hz (so over three decades only). The data of Fig. 19 shows a linear trend with a slope $\alpha = 4.06$ ($R^2 = 0.96$). In this case, $\ln(A) = \ln(10^3)$ and hence, a slope of $\alpha = 4.40$ is expected from Eq. (17).

We can now use $\alpha = 4.06$ in $M_n = -\alpha\sigma''$ and the trend shown in Fig. 17 (with $\rho_g = 3000$ kg m^{-3}), we obtain $\lambda(Na^+, 25\ °C) = 3.46 \times 10^{-10}$ m^{-2} s^{-1} V^{-1} (consistent with $R = \lambda/B = 0.084$). The partition coefficient and the mobility of the counterions in the Stern layer can be obtained as (Revil et al., 2017a),

$$f = 1 - \frac{B}{\beta_{(+)}}(1-R). \tag{28}$$

Using $R = 0.22$, $\beta_{(+)}(Na^+, 25\ °C) = 5.2 \times 10^{-8}$ m^{-2} s^{-1} V^{-1} we obtain $f = 0.94$ i.e., 94% of the counterions are located in the Stern layer. This value is consistent with that obtained in Revil et al. (2017a) for basalts where we obtained $f = 0.93$. Finally, the mobility of the counterions in the Stern layer is given by (Revil et al., 2017a),

$$\beta^S_{(+)} = \beta_{(+)}\frac{R(1-f)}{f(1-R)}. \tag{29}$$

Using the previous values of the parameters involved in Eq. (26) ($R = 0.22$, $\beta_{(+)}(Na^+, 25\ °C) = 5.2 \times 10^{-8}$ m^{-2} s^{-1} V^{-1}, $f = 0.94$), this yields $\beta^S_{(+)}(Na^+, 25\ °C) = 9.4 \times 10^{-10}$ m^{-2} s^{-1} V^{-1}.

5.5. Influence of temperature

The influence of temperature was investigated on two core samples using the temperature range 5–50 °C and with a salinity corresponding to a pore water conductivity of 0.2 S m^{-1} (NaCl, 20 °C). The spectra are shown in Fig. 21. The magnitude of both the quadrature conductivity and the in-phase conductivity increases with the temperature. Fig. 22 shows that this increase can be fitted with an Arrhenius law with the same activation energy for the bulk and surface conductivities and polarization processes, i.e., $E_a^w = E_a^S = 16.3 \pm 0.5$ kJ Mol^{-1}. This activation energy is consistent with the activation energy for the viscosity of the water molecules as explained in Section 2.3.

5.6. Influence of pyrite content

Volcanic areas can also contain sulfide deposits and other metallic (in a broad sense) deposits. As mentioned above the pyrite grains are mixed with the same background (crushed) volcanic rock (Sample MERTurist). The spectra are shown in Fig. 23. As expected, we see clearly on these spectra that the presence of pyrite increases the normalized chargeability and the quadrature conductivity of the mixtures. The chargeability is determined between the frequency 10 mHz and 10 kHz and plotted as a function of the volumetric content of pyrite in Fig. 24. A comparison between the experimental data and the prediction of Eq. (22) (no fitting parameters, plain line) is shown in Fig. 24. There is an excellent agreement between the theory and the experimental data.

6. Application to a synthetic tomographic test

In this section, we explain how induced polarization tomography can assist electrical conductivity tomography and show the type of images the method can produce for a volcano. As mentioned in Section 2, the electrical conductivity has two contributions (see Eq. (5) and Fig. 14): a bulk contribution associated with conduction in the pore network and surface contribution associated with the conduction path in the electrical double layer. Time-domain induced polarization can be used to image the normalized chargeability, which in turn can be related

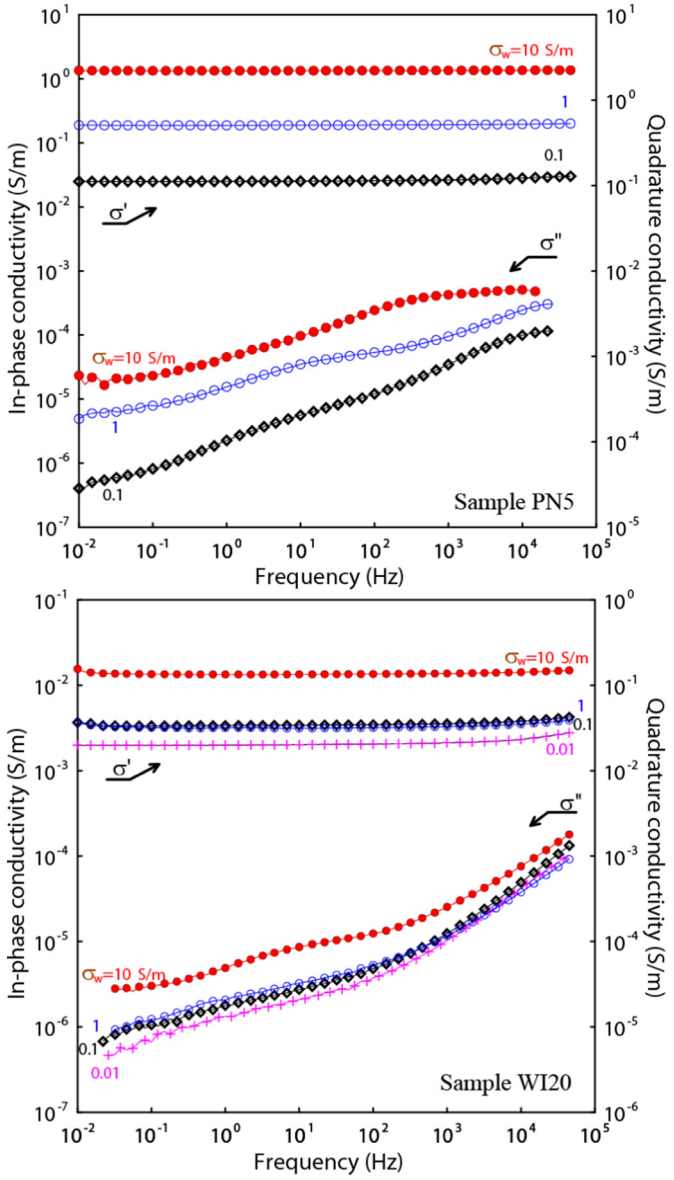

Fig. 12. Spectral induced polarization data for two volcanic samples from White Island in the frequency range 10 mHz–45 kHz. a. Complex conductivity spectrum of core sample PN5. b. Complex conductivity spectrum of core sample WI20SIP. The induced polarization measurements are performed at different pore-water conductivities 0.01, 0.1, 1 and 10 Sm^{-1} (NaCl, 25 °C). The quadrature conductivity is here taken positive to plot this quantity on a log scale.

to the surface conductivity using $\sigma_S^{\infty} = M_n/R$ (see Eq. (18)) where R is a universal constant independent of temperature and saturation. Therefore, surface conductivity can be determined from normalized chargeability, and the conductivity can be decomposed into its two contributions.

We examine now how a combined conductivity/induced polarization survey could be conducted at a volcano using a synthetic case. We use conditions that are representative of real field conditions, especially with the recent development of new equipment such as the FullWaver instrument from IRIS. Such equipment is designed to perform large-scale conductivity and induced polarization surveys reaching a depth of investigation as deep as 1.5 km.

For this study, 10 parallel profiles separated by 786 m from each other were used with 32 electrodes per profile (therefore a total of 320 electrodes are simulated). Along a profile, the distance between two electrodes is 380 m. Fig. 25 shows the position of the electrodes together with the tetrahedral finite element mesh used for the forward and inverse simulations. The synthetic volcano is composed of three main parts. (1) a magmatic chamber connected to the surface by a conduit (electrical conductivity $10^{-0.5}$ S m^{-1}, normalized chargeability $10^{-4.5}$ S m^{-1}), (2) an altered region located on one flank of the volcano (conductivity $10^{-3.5}$ S m^{-1}, normalized chargeability 10^{-3} S m^{-1}), and (3) the remaining part of the volcanic edifice (conductivity 10^{-2} S m^{-1}, normalized chargeability $10^{-5.5}$ S m^{-1}). The true distributions of the electrical conductivity and normalized chargeability are shown in Figs. 26a and 27a, respectively.

The network of electrodes at the ground surface of the volcano is used to simulate a geoelectrical survey. All the measurements were acquired using a dipole-dipole configuration resulting in 2160 apparent conductivity measurements and 2160 apparent chargeability measurements. All the collected data are corrupted with a Gaussian noise of 5% to simulate data error. The goal of the geophysical inverse problem is to image the true distributions of the electrical conductivity and the normalized chargeability (the true fields are assumed of course unknown and we estimate them from the measured data). This problem is mathematically formulated as an inverse problem. As this inverse problem is ill-posed, its solution is non-unique and therefore we need to apply some constraints on the desired solution to ensure that the inverse scheme converges towards the most optimal electrical conductivity and normalized chargeability, while honoring the data such that we arrive at a physically meaningful model. The mathematical background required for solving the inverse problem is well-established (see for instance Tikhonov and Arsenin, 1977) and will not be presented in the current contribution (see for instance Johnson et al., 2010, for the electrical conductivity problem applied to volcanoes and Soueid Ahmed et al., 2018a, 2018b, for the inverse problem in time-domain induced polarization).

To produce the 3D tomographies of the estimated parameters, we use a 3D code (written in Matlab) discussed and benchmarked in Soueid Ahmed et al. (2018a, 2018b). We discretize the simulation domain into 52,188 tetrahedral cells. A parameter value is assigned to each of these cells. As we know true distributions of the conductivity and normalized chargeability, it will be easy to check the correctness of the estimated tomograms by comparing them to the true distributions. Fig. 26b shows the tomogram of the inverted electrical conductivity. One can easily notice that the main units of the volcano: the conduit, the altered area, and the host rock are well-reconstructed both in terms of delineation of the features and the magnitude of the electrical conductivity. The magmatic chamber is almost not recovered because of the lack of sensitivity at depth for the survey used here. Fig. 27b shows the inverted normalized chargeability. The altered area on the flank of the volcano is clearly imaged with the same order of magnitude as the true one. Then, combining the conductivity and normalized chargeability tomograms and the petrophysics developed in the current paper for volcanic rocks, we can invert for the porosity and some alteration proxies. Case studies will be discussed in a future contribution.

7. Conclusions

We investigated the complex conductivity of a set of 85 volcanic rock samples from five volcanoes located in Indonesia, Portugal, USA, and New Zealand in order to provide answers to 6 fundamental questions. We recall here these questions and we summarize their answers found in this work.

(1) Is the relationship developed in a previous paper for basaltic rocks valid for all types of volcanic rocks? The response is clearly yes as the new data agree with the results obtained on basalts (from Hawaii) and sedimentary rocks. We obtain therefore universal trends.
(2) Is the cation exchange capacity (CEC) a proxy of the alteration of the volcanic rocks? We found that the CEC is directly proportional

Table 4
Relevant petrophysical of the 26 core samples from Yellowstone National Park in the USA. The quantity ρ_g denotes the grain density (kg m^{-3}), ϕ the connected porosity (dimensionless), F the electrical (intrinsic) formation factor (dimensionless), CEC (expressed in meq/100 g) denotes the cation exchange capacity, and σ'' (in Sm^{-1}) denotes the quadrature conductivity at 1 Hz. The sandstone, coarse sandstone and conglomerate are glacial deposits.

Sample	ϕ (−)	ρ_g (kg m^{-3})	F (−)	CEC (meq/100 g)	σ_S (10^{-4} S m^{-1})	σ'' (10^{-5} S m^{-1})	Comment
16YS01	0.333	2236	11	1.762	6.7	1.5	Sandstone
16YS02	0.289	1887	88	1.026	9.7	–	Conglomerate
16YS03	0.282	2201	34	1.726	6.3	1.2	Conglomerate
16YS03B	0.236	2006	32	0.642	2.9	0.6	Conglomerate
16YS04	0.377	2153	10	1.335	38.8	1.9	Sandstone
16YS05	0.330	2400	20	0.731	33.6	0.6	Sandstone
16YS06	0.296	1921	65	0.300	24.4	–	Conglomerate
16YS07	0.192	2188	28	1.624	10.0	–	Coarse sandstone
16YS08	0.388	2169	9	2.002	41.8	5.1	Sandstone
16YS09	0.242	2139	65	0.727	–	0.2	Coarse sandstone
16YS10	0.193	2640	73	2.279	12.7	0.8	Coarse sandstone
16YS11	0.326	2049	32	0.930	4.6	0.3	Conglomerate
16YS13	0.281	2185	16	1.888	–	0.7	Conglomerate
16YS14	0.140	1871	99	1.112	7.2	–	Sandstone
Y2-89a	0.130	2381	102	10.107	213.3	19.5	Rhyolite breccia
Y2-230a	0.083	2532	657	0.605	0.6	0.3	Rhyolite breccia
Y2-233a	0.296	2273	32	12.087	189.7	38.8	Rhyolite breccia
Y2-460a	0.226	2547	69	1.779	39.8	10.9	Rhyolite vitrophyric
Y2-479a	0.231	2573	32	1.849	23.8	9.2	Rhyolite vitrophyric
Y8-168a	0.295	2645	32	1.839	10.8	3.9	Sandstone and conglomerate
Y8-189a	0.119	2213	500	8.593	85.5	6.6	Rhyolite vitrophyric
Y8-197a	0.201	2302	55	7.472	149.4	15.5	Rhyolite vitrophyric
Y8-198a	0.113	2387	152	6.444	102.2	3.6	Rhyolite vitrophyric
Y8-204.8a	0.176	2338	30	7.343	116.6	10.0	Rhyolite vitrophyric
Y8-209a	0.480	2082	9	11.116	337.5	105.3	Pumiceous Tuff
Y8-216.2a	0.532	2287	9	7.167	289.8	127.8	Pumiceous Tuff

to the specific surface area of volcanic rocks. Therefore CEC can be considered as a proxy of alteration.

(3) How do the surface and quadrature conductivities of volcanic rocks depend on their cation exchange capacity (CEC) and specific surface area? The surface conductivity increases with the degree of alteration of the volcanic rocks as expected. Alteration strongly affects the induced polarization parameters such as quadrature conductivity.

(4) How can the quadrature conductivity and the normalized chargeability be related to each other? Normalized chargeability is found to be proportional to the quadrature conductivity so the normalized chargeability is also related to the alteration of volcanic rocks. The cation exchange capacity is found to be proportional to the specific surface area, a known proxy of alteration of volcanic rocks, at least in some classical alteration paths producing clay and zeolite minerals.

(5) How is the polarization affected by temperature and the volume content of metallic particles? The magnitude of the quadrature conductivity and electrical conductivity increases with the temperature with the same activation energy (around 16 kJ Mol^{-1}).

Table 5
Relevant petrophysical of the 22 core samples from Whakaari volcano (White Island) in New Zealand. The quantity ρ_g denotes the grain density (kg m^{-3}), ϕ the connected porosity (dimensionless), F the electrical (intrinsic) formation factor (dimensionless), CEC (expressed in meq/100 g) denotes the cation exchange capacity, σ'' (in Sm^{-1}) denotes the quadrature conductivity at 1 Hz, S_{sp} corresponds to the specific surface area measured with the BET technique, and k is the permeability (measured at a confining pressure of 1 MPa; data from Heap et al., 2017).

Sample	ϕ (−)	ρ_g (kg m^{-3})	F (−)	CEC (meq/100 g)	S_{sp} (m^2/g)	σ_S (10^{-4} S m^{-1})	σ''(10^{-5} S m^{-1})	k (m^2)	Type
3	0.555	2145	7	0.686	–	16.8	1.5	1.00×10^{-16}	Lithified ash tuff
4	0.399	2182	66	0.767	–	13.7	0.3	1.94×10^{-15}	Lithified ash tuff
34	0.500	2160	8	0.812	–	14.3	1.3	3.01×10^{-13}	Lithified ash tuff
55	0.437	2235	9	0.341	–	4.8	0.8	9.42×10^{-13}	Lithified ash tuff
67	0.496	2152	8	0.469	–	12.0	0.6	4.98×10^{-13}	Lithified ash tuff
70	0.461	2231	8	1.152	–	13.6	0.2	1.52×10^{-12}	Lithified ash tuff
78	0.436	2204	28	0.514	–	25.8	1.1	3.61×10^{-15}	Lithified ash tuff
91	0.308	2242	16	0.810	–	15.9	1.1	1.65×10^{-12}	Lava breccia
99	0.129	2084	190	0.811	–	1.4	0.1	2.79×10^{-14}	Lava breccia
102	0.197	2240	19	0.426	–	76.1	0.4	5.55×10^{-13}	Lava breccia
105	0.269	2223	190	0.342	–	5.1	0.2	1.28×10^{-14}	Lava breccia
107	0.261	2320	36	0.727	–	15.0	1.5	6.69×10^{-13}	Lava breccia
110	0.374	2410	25	0.727	–	31.9	0.6	8.62×10^{-18}	Lithified ash tuff
111	0.436	2255	10	0.684	–	5.5	0.6	2.90×10^{-13}	Lava breccia
112	0.357	2290	15	1.320	–	12.7	1.1	2.38×10^{-16}	Lithified ash tuff
115	0.484	2167	13	0.643	–	14.3	1.4	4.33×10^{-15}	Lithified ash tuff
116	0.405	3171	26	1.409	–	12.6	0.7	2.51×10^{-13}	Lava breccia
W120	0.059	2686	1027	2.818	15.8	24.2	1.8	7.05×10^{-17}	Andesitic lava
W121	0.358	2240	23	0.812	4.4	4.7	0.8	1.27×10^{-16}	Lithified ash tuff
W122	0.448	2022	15	0.215	3.9	13.9	1.2	3.14×10^{-15}	Lithified ash tuff
W123	0.420	2244	13	1.890	11.4	19.3	3.6	1.21×10^{-15}	Lithified ash tuff
W124	0.466	2115	8	0.428	4.6	11.9	1.5	3.08×10^{-13}	Lithified ash tuff

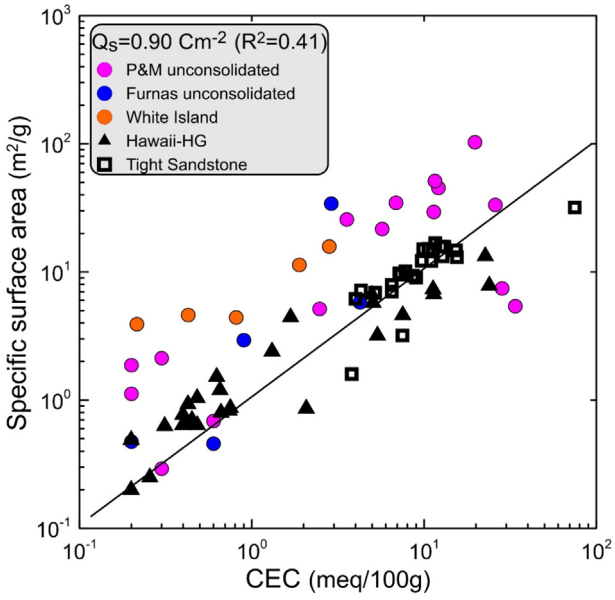

Fig. 13. Relationship between specific surface area and cation exchange capacity (CEC) for the consolidated and unconsolidated volcanic rock samples investigated in the present study. The surface charge density of the mineral surface is defined as the ratio between the CEC and the specific surface area. The linear trend (in a log-log plot) is used to determine the average surface charge density of the mineral surface, which corresponds here to ~6 elementary charges per nm^2 ($Q_S = 0.90 \pm 0.10$ C m^{-2}). The tight sandstones are from the study by Revil et al. (2018) and are not used for the fit. "P&M unconsolidated" correspond to the unconsolidated core samples from Papandayan and Merapi volcanoes. This shows that the CEC of a volcanic rock ca be considered as a proxy of alteration.

Chargeability of volcanic rocks can be decomposed in the sum of two terms: a contribution associated with the volume content (independent of temperature) of metallic particles and the background polarization of the matrix around the metallic grains (also independent of temperature).

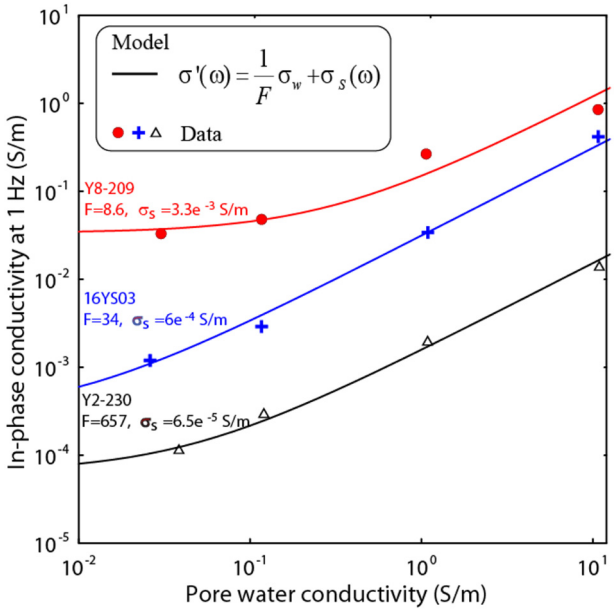

Fig. 14. Relationship between In-phase conductivity σ' and pore water conductivity σ_w for three core samples from Yellowstone Park (USA). We plot the conductivity of the rock sample (at 1 Hz) as a function of the conductivity of the pore water at four different pore water salinities. Then, we used Eq. (5) to determine the (intrinsic) formation factor F and surface conductivity σ_s from the linear regression of the data. These values are reported in Tables 1 to 5.

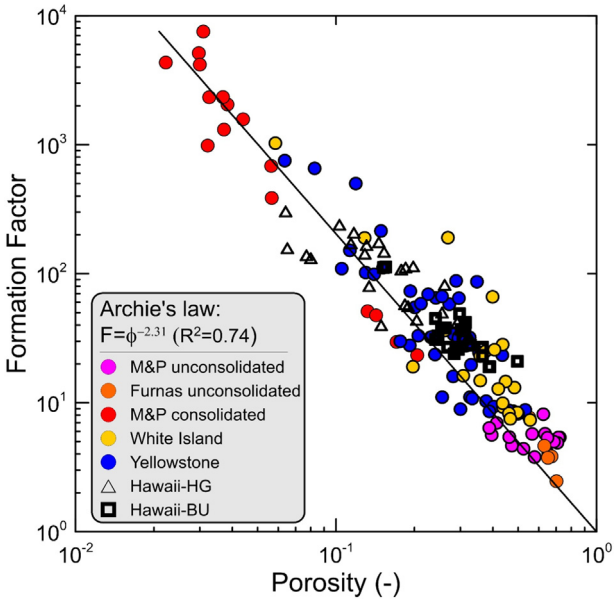

Fig. 15. The intrinsic formation factor (i.e., corrected for surface conductivity) F versus the connected porosity ϕ for the volcanic rocks used in this study. We fit the data with Archie's law $F = \phi^{-m}$, where the cementation exponent m is dimensionless. This figure shows that al volcanic rocks can be plotted on a unique trend.

(6) Can we image electrical conductivity and normalized chargeability of a volcanic edifice and offer a combined approach to interpret these data? Electrical conductivity alone cannot be used to interpret volcanic structures because we cannot separate the bulk conductivity (associated with conduction in the pore network) from the surface conductivity associated with alteration. Fortunately, induced polarization can provided the required information to allow

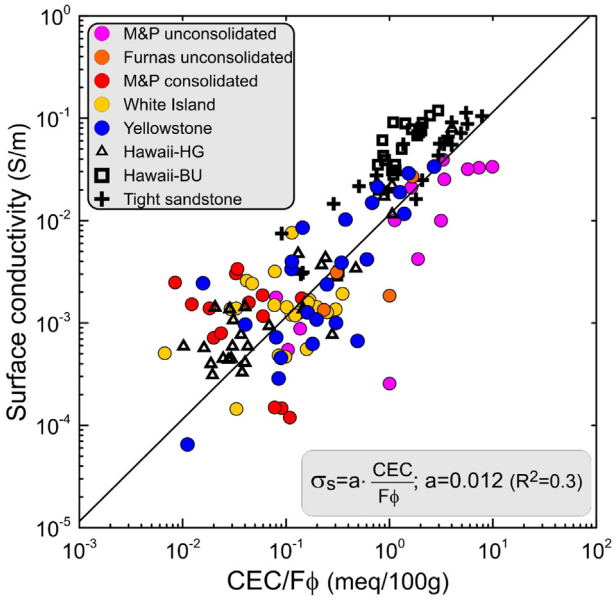

Fig. 16. The surface conductivity (expressed in S m^{-1}) versus the normalized cation exchange capacity defined by CEC/$F\phi$ where CEC denotes the cation exchange capacity (expressed here in meq/100 g, F the formation factor, and ϕ the connected porosity). Note that the CEC is usually reported in meq/100 g but expressed in C kg^{-1} in the international system of units, 1 meq/(100 g) = 963.2 C kg^{-1}. The volcanic rock data are contrasted with the tight sandstones data from Revil et al. (2018). Only the volcanic rocks from the present study are used for the fit. This figure shows that al volcanic rocks can be plotted on a unique trend.

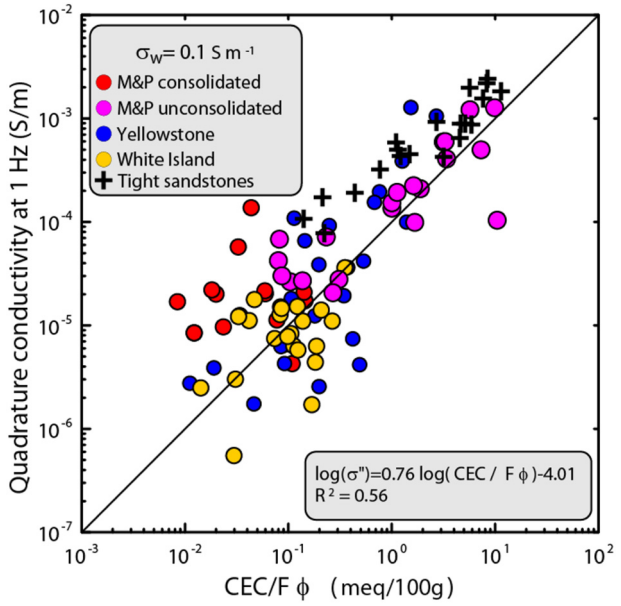

Fig. 17. Relationship between the quadrature conductivity (at a pore-water conductivity of approximately 0.1 Sm^{-1} and taken at 1 Hz) and normalized CEC (i.e., the CEC divided by the tortuosity of the bulk pore space). The quadrature conductivity is here taken positive to plot this quantity on a log scale. The tortuosity of the bulk pore space determined as the product of the (intrinsic) formation factor by the (connected) porosity (1 meq/(100 g) = 963.2 C kg^{-1}). M&P stands for the Merapi and Papandayan volcanoes in Indonesia. The volcanic rock data are contrasted with the tight sandstones data from Revil et al. (2018). Only the volcanic rocks are used for the fit. This figure shows that al volcanic rocks can be plotted on a unique trend.

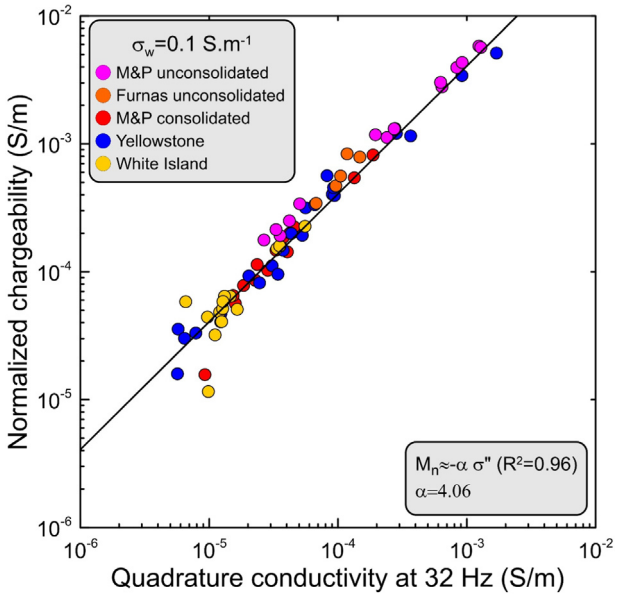

Fig. 19. Linear relationship between normalized chargeability (determined between 1 Hz and 1 kHz as the difference in the in-phase conductivity) and the quadrature conductivity (at the geometric mean frequency of 32 Hz) for the volcanic samples at a pore water conductivity of 0.1 S m^{-1} (NaCl, 25 °C). The plain line corresponds to the best fit of the data using a linear model between the normalized chargeability and the quadrature conductivity. The quadrature conductivity is here taken positive to plot this quantity on a log scale. The measured slope ($\alpha = 4.06$) can be compared with the predicted slope of $\alpha = 4.40$ as discussed in the main text (see Eq. (17)). The normalized chargeability is found to be proportional to the quadrature conductivity so the normalized chargeability is also related to the alteration of volcanic rocks.

us to separate the two conductivity contributions. Indeed, induced polarization parameters (such as the normalized conductivity and the quadrature conductivity) are directly proportional to the surface conductivity. That said, the presence of pyrite can increase substantially the polarization of the mixture. This increase can be predicted from the theory.

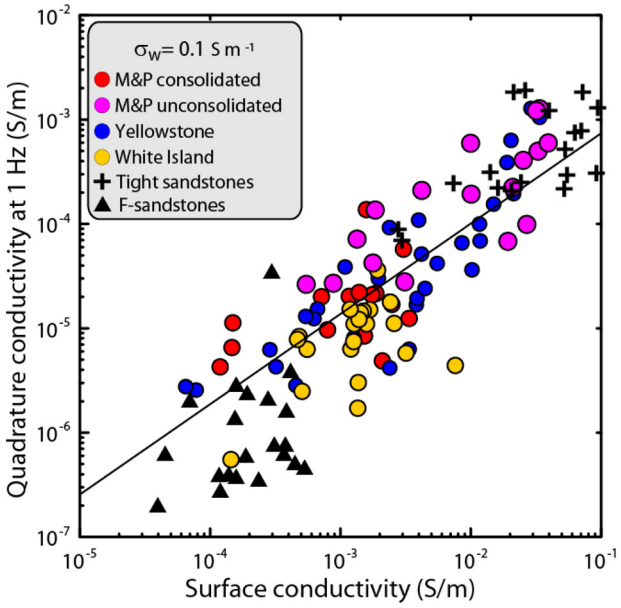

Fig. 18. Quadrature conductivity versus surface conductivity (at a pore-water conductivity of approximately 0.1 Sm^{-1} and taken at 1 Hz) for volcanic rocks. The quadrature conductivity is here taken positive to plot this quantity on a log scale. Note that this trend is independent of the value of the formation factor and electrical tortuosity, saturation, and temperature. The volcanic rock data are contrasted with the tight sandstones data from Revil et al. (2018) and the F-sandstones (Fontainebleau sandstones) investigated by Revil et al. (2014). The F-sandstones are clay-free sandstones. Only the volcanic rocks are used for the fit. This figure shows that al volcanic rocks can be plotted on a unique trend.

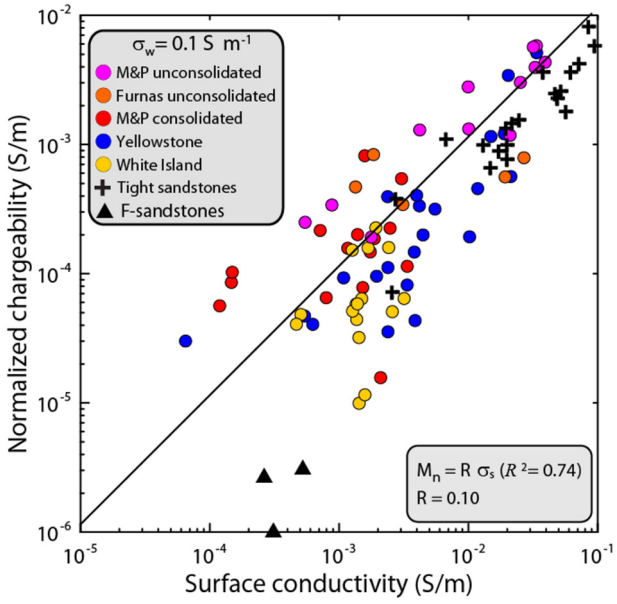

Fig. 20. Linear relationship between normalized chargeability (determined between 1 Hz and 1 kHz as the difference in the in-phase conductivity, 0.1 S m^{-1}, NaCl, 25 °C) and the surface conductivity for the volcanic samples at. The plain line corresponds to the best fit of the data using a linear model between the normalized chargeability and the surface conductivity. The measured slope leads to $R = 0.10$. The volcanic rock data are contrasted with the tight sandstones data from Revil et al. (2018) and the F-sandstones (Fontainebleau sandstones) investigated by Revil et al. (2014). Only the volcanic rocks are used for the fit.

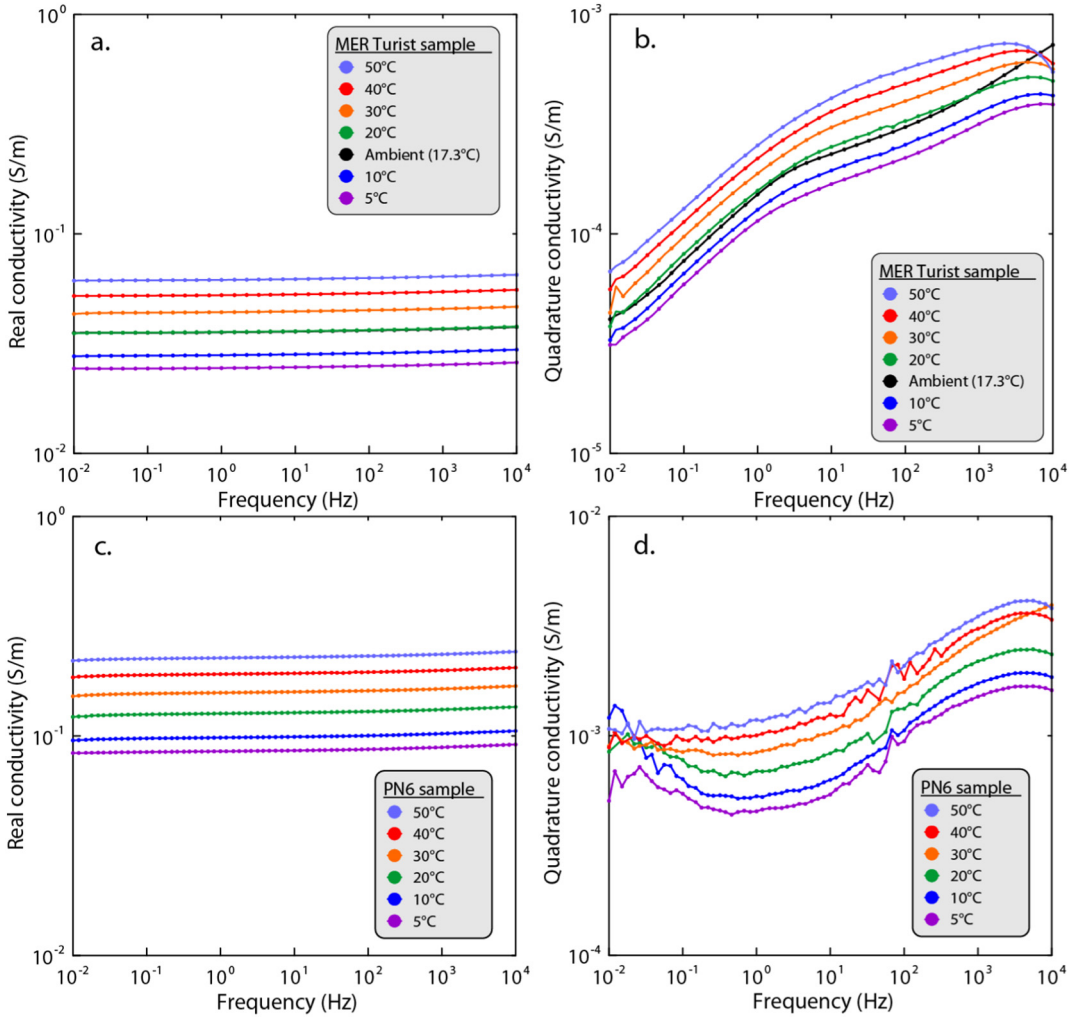

Fig. 21. Temperature dependence of the complex conductivity spectra of two core samples (MER Turist and PN6). a. In-phase conductivity for the core sample MER Turist. b. Quadrature conductivity for the core sample MER Turist. The spectrum labeled "ambient temperature" was performed outside the temperature-controlled bath at the room temperature of 17.3 °C. c. In-phase conductivity for the core sample PN6. d. Quadrature conductivity for the core sample PN6. The conductivity of the pore water was 0.2 S m^{-1} (NaCl, 20 °C). The quadrature conductivity is here taken positive to plot this quantity on a log scale. The ambient temperature measurements were carried out outside the temperature-controlled bath.

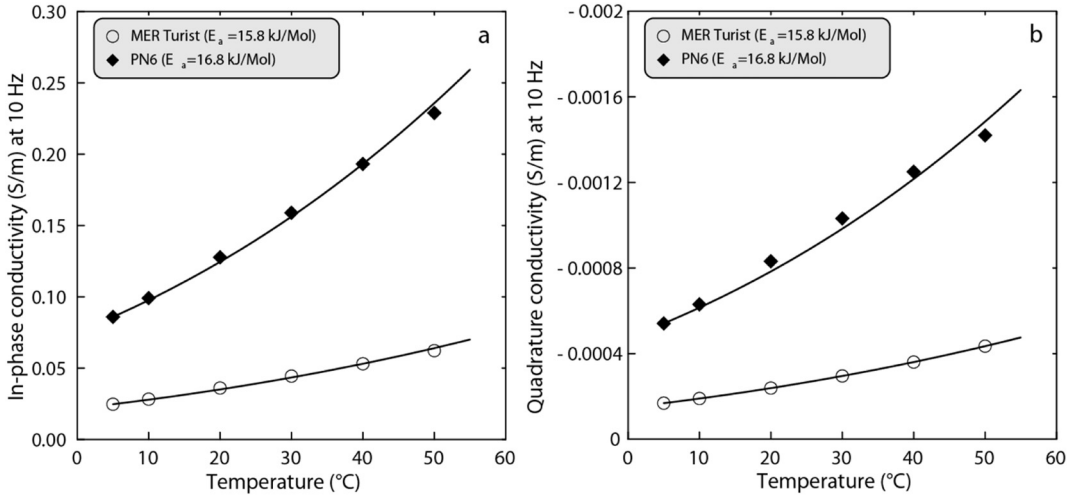

Fig. 22. Temperature dependence of the in-phase and quadrature conductivities of two core samples (MER Turist and PN6) at 10 Hz (a typical frequency used for field studies). a. In-phase conductivity versus temperature for the two core samples. b. In-phase conductivity versus temperature for the two core samples. The activation energy is close to the activation energy of the viscosity of the pore water (15–16 kJ Mol^{-1}). This provides a way to correct conduction and polarization parameters from the effect of temperature.

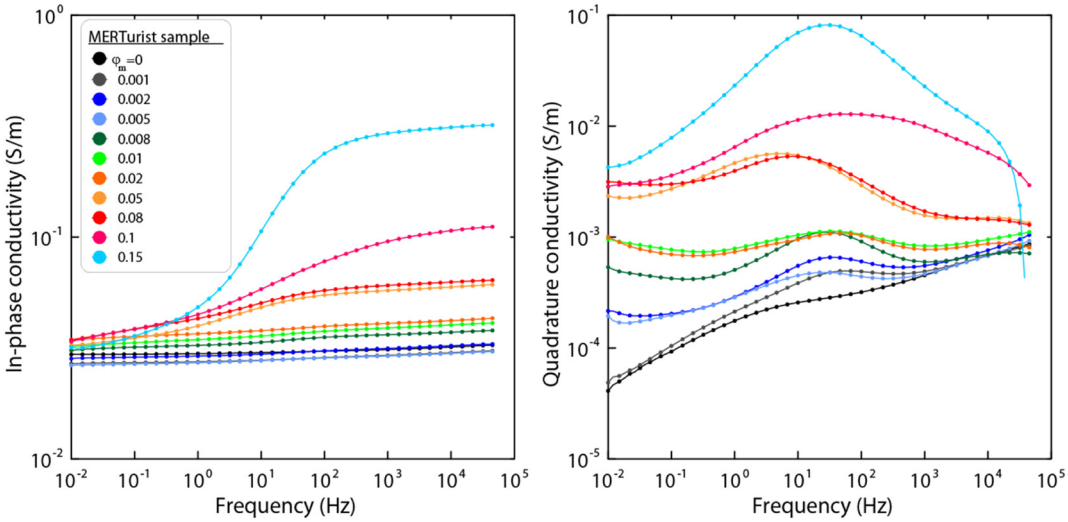

Fig. 23. Influence of the volume content of pyrite φ_m on the complex conductivity spectra (in-phase and quadrature components) of the pyrite/volcanic rock mixtures (the background volcanic rock corresponds to the MERTurist core sample, black symbols). The quadrature conductivity is here taken positive to plot this quantity on a log scale. The measurements with $\varphi_m = 0$ represent the spectra of the background material.

A recently developed forward/inverse finite element modeling code is used to illustrate how electrical conductivity and normalized chargeability can be image on a volcanic edifice. The two methods can be used in concert to map the alteration on the flank of a volcanic structure. Since hydrothermal alteration can influence (1) outgassing and therefore explosivity (e.g., Edmonds et al., 2003; Ball et al., 2015; Heap et al., 2017) and (2) flank, dome and crater rim stability (e.g., Reid et al., 2001; Finn et al., 2001; Reid, 2004; Rosas-Carbajal et al., 2016; Marmoni et al., 2017; Cook et al., 2017), alteration maps of active volcanoes, using the methodology outline herein, will emerge as a powerful tool in volcano monitoring and geohazard mapping.

Acknowledgements

M. J. Heap thanks the Buttle family, Pee Jay Tours, GNS Science, and all those that helped collect the materials from Whakaari volcano (particularly B. Kennedy). We thank the USGS Core research Center in Denver, Colorado for allowing us to sample Yellowstone drill cores Y-2 and Y-8. The field samples at Yellowstone were collected under the research permit YELL-2016-SCI-7006. The research at Yellowstone was funded by Labex OSUG@2020 (ANR10 LABX56) and CNRS-INSU program SYSTER. We thank François Beauducel, Mochammad Husni Rizal, and Shaul Hurwitz for fruitful discussions, and A. Bayu Adji, S. Sumarti, A.

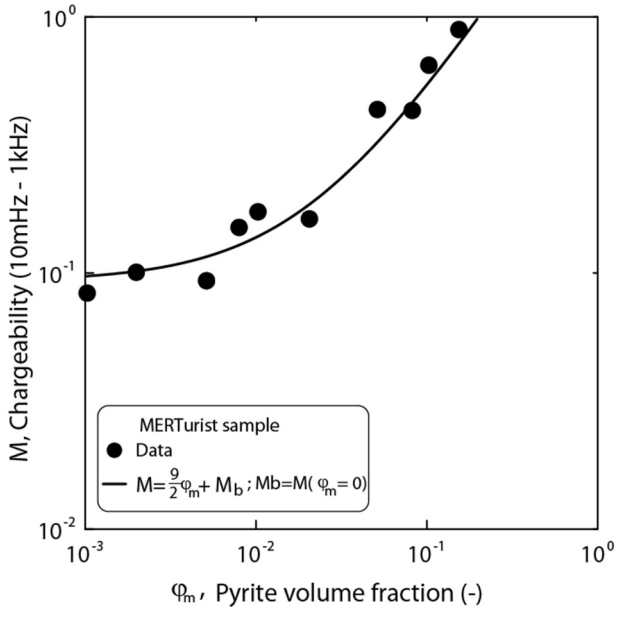

Fig. 24. Influence of the volume content of pyrite φ_m on the chargeability M of the pyrite volcanic rock mixtures (the background volcanic rock corresponds to the MERTurist core sample). The plain line corresponds to the prediction of the theory (no fitting parameters). Note that at low salinity, $M_b \approx R = 8 \times 10^{-2}$. This provides a way to correct polarization from the effect of the volume content of metallic particles (pyrite and magnetite).

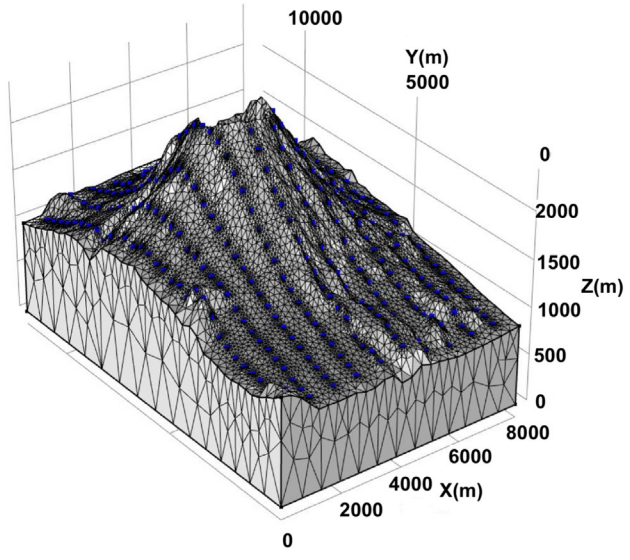

Fig. 25. Geometry and mesh for the synthetic test. The domain of interest was discretized into 52,188 elements. The blue dots denote the positions of the 320 electrodes used in the simulation. One can observe that the mesh is refined around the electrodes. This is done to increase the numerical accuracy during the forward modeling step. We simulate an acquisition survey with 2160 apparent conductivities and 2160 apparent chargeability measurements, which corresponds to a modest amount of data. The same mesh is used for the forward and inverse modeling. (For interpretation of the references to color in this figure legend, the reader is referred to the web version of this article.)

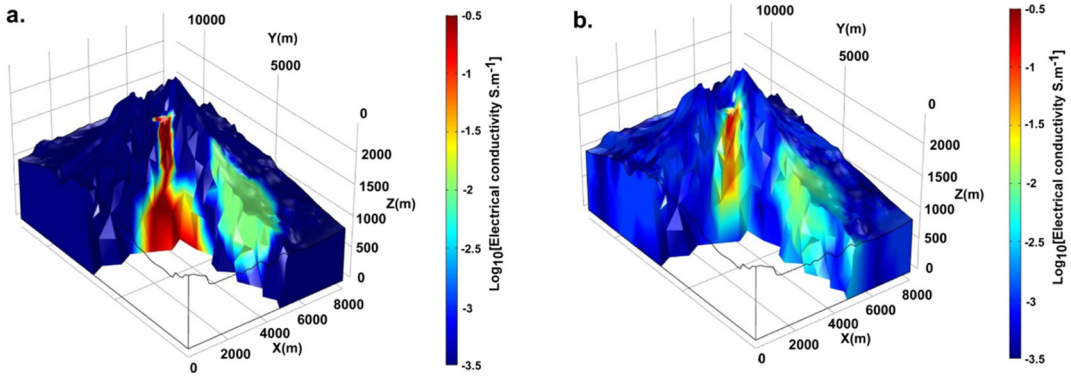

Fig. 26. Electrical conductivity tomography. a. True electrical conductivity distribution showing two conductive zones around the conduit and the magmatic chamber and an altered zone on one flank of the volcano. b. Estimated electrical conductivity distribution obtained by tomography (fourth iteration). The sensitivity is too low to image the magmatic chamber at depth but the altered flank is well imaged.

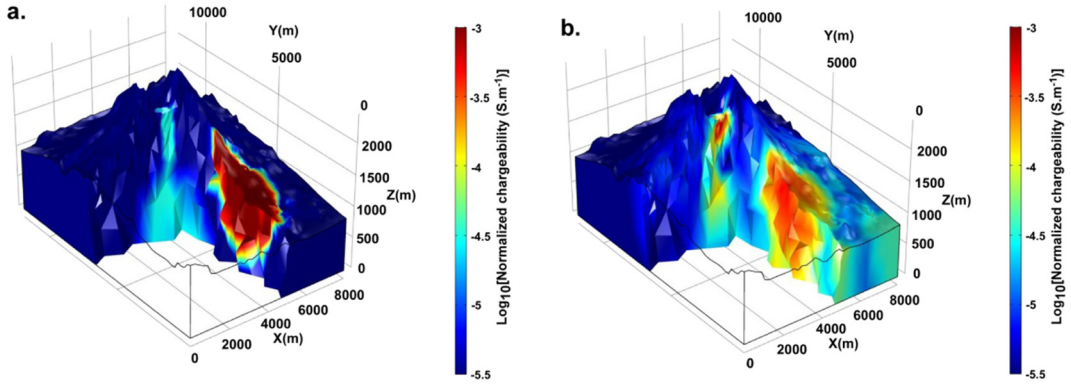

Fig. 27. Normalized chargeability tomography. a. True normalized chargeability distribution showing two chargeable zones around the conduit and the magmatic chamber and an altered zone on one flank of the volcano. b. Estimated normalized chargeability distribution (fourth iteration). The altered flank of the volcano is relatively well-imaged.

Riyan, B. Santoso and S. Widodo for the mineralogical analysis of the rock samples from Indonesia, H. Humaida for the core samples from Merapi, and M. Frichnel for her help with the measurements with the core samples from Merapi and Papadayan. We thank E. Zimmermann for the quality of his instrument. We thank the two referees and the Editor for their comments and professional handling of our manuscript.

References

Aran, D., Maul, A., Masfaraud, J., 2008. A spectrophotometric measurement of soil cation exchange capacity based on cobaltihexamine chloride absorbance. Compt. Rendus Geosci. 340 (12):865–871. https://doi.org/10.1016/j.crte.2008.07.015.

Archie, G.E., 1942. The electrical resistivity log as an aid in determining some reservoir characteristics. Petroleum. Trans. AIME 146:54–62. https://doi.org/10.2118/942054-G.

Asmoro, P., Wachyudin, D., Mulyadi, E., 1989. Geological Map of Papandayan Volcano, Garut, West Java, Scale 1:25.000. Volcanological Survey of Indonesia.

Ball, J.L., Stauffer, P.H., Calder, E.S., Valentine, G.A., 2015. The hydrothermal alteration of cooling lava domes. Bull. Volcanol. 77 (12):102. https://doi.org/10.1007/s00445-015-0986-z.

Bargar, K.E., Beeson, M.H., 1981. Hydrothermal alteration in research drill hole Y-2, Lower Geyser Basin, Yellowstone National Park, Wyoming. Am. Mineral. 66, 473–490.

Beeson, M.H., Bargar, K.E., 1984. Major and Trace Element Analyses of Drill Cores From Thermal Areas in Yellowstone National Park, Wyoming (No. 84-373). US Geological Survey.

Bernard, M.-L., Zamora, M., Géraud, Y., Boudon, G., 2007. Transport properties of pyroclastic rocks from Montagne Pelée volcano (Martinique, Lesser Antilles). J. Geophys. Res. 112:B05205. https://doi.org/10.1029/2006JB004385.

Bleil, D.F., 1953. Induced polarization, a method of geophysical prospecting. Geophysics 18:636–661. https://doi.org/10.1190/1.1437917.

Bonnet, A.-L., Corriveau, L., 2007. Alteration vectors to metamorphosed hydrothermal systems in gneissic terranes. In: Goodfellow, W.D. (Ed.), Mineral Deposits of Canada—A Synthesis of Major Deposit-Types, District Metallogeny, the Evolution of Geological Provinces, and Exploration Methods. Geological Association of Canada, Mineral Deposits Division, Special Publication No. 5, pp. 1035–1049.

Börner, F.D., 1992. Complex conductivity measurements of reservoir properties. Proc Third European Core Analysis Symposium, Paris, pp. 359–386.

Brunauer, S., Emmett, P.H., Teller, E., 1938. Adsorption of gasses in multimolecular layers. J. Am. Chem. Soc. 60 (2):309–319. https://doi.org/10.1021/ja01269a023.

Christiansen, R.L., 2001. The Quaternary and Pliocene Yellowstone Plateau Volcanic Field of Wyoming, Idaho, and Montana (No. 729-G).

Ciesielski, H., Sterckemann, T., 1997. Determination of exchange capacity and exchangeable cations in soils by means of cobalt hexamine trichloride. Effects of experimental conditions. Agronomie 17:1–7. https://doi.org/10.1051/agro:19970101.

Colombier, M., Wadsworth, F.B., Gurioli, L., Scheu, B., Kueppers, U., Di Muro, A., Dingwell, D.B., 2017. The evolution of pore connectivity in volcanic rocks. Earth Planet. Sci. Lett. 462:99–109. https://doi.org/10.1016/j.epsl.2017.01.011.

Cook, S.C., Kennedy, B.M., Villeneuve, M.C., 2017. Engineering geology model of the Crater Lake outlet, Mt. Ruapehu, New Zealand, to inform rim breakout hazard. J. Volcanol. Geotherm. Res. 350:69–83. https://doi.org/10.1016/j.jvolgeores.2017.12.006.

Day, S.J., 1996. Hydrothermal pore fluid pressure and the stability of porous, permeable volcanoes. Geol. Soc. Lond., Spec. Publ. 110 (1):77–93. https://doi.org/10.1144/GSL.SP.1996.110.01.06.

Edmonds, M., Oppenheimer, C., Pyle, D.M., Herd, R.A., Thompson, G., 2003. SO_2 emissions from Soufriere Hills volcano and their relationship to conduit permeability, hydrothermal interaction and degassing regime. J. Volcanol. Geotherm. Res. 124 (1–2): 23–43. https://doi.org/10.1016/S0377-0273(03)00041-6.

Erdmann, S., Martel, C., Pichavant, M., Kushnir, A., 2014. Amphibole as an archivist of magmatic crystallization conditions: problems, potential, and implications for inferring magma storage prior to the paroxysmal 2010 eruption of Mount Merapi, Indonesia. Contrib. Mineral. Petrol. 167 (6):1016. https://doi.org/10.1007/s00410-014-1016-4.

Erdmann, S., Martel, C., Pichavant, M., Bourdier, J.L., Champallier, R., Komorowski, J.C., Cholik, N., 2016. Constraints from phase equilibrium experiments on pre-eruptive storage conditions in mixed magma systems: a case study on crystal-rich basaltic andesites from Mount Merapi, Indonesia. J. Petrol. 57 (3):535–560. https://doi.org/10.1093/petrology/egw019.

Farquharson, J., Heap, M.J., Varley, N.R., Baud, P., Reuschlé, T., 2015. Permeability and porosity relationships of edifice-forming andesites: a combined field and laboratory study. J. Volcanol. Geotherm. Res. 297:52–68. https://doi.org/10.1016/j.jvolgeores.2015.03.016.

Finn, C.A., Sisson, T.W., Deszcz-Pan, M., 2001. Aerogeophysical measurements of collapse-prone hydrothermally altered zones at Mount Rainier volcano. Nature 409 (6820): 600–603. https://doi.org/10.1038/35054533.

Frolova, J., Ladygin, V., Rychagov, S., Zukhubaya, D., 2014. Effects of hydrothermal alterations on physical and mechanical properties of rocks in the Kuril–Kamchatka island arc. Eng. Geol. 183:80–95. https://doi.org/10.1016/j.enggeo.2014.10.011.

Giggenbach, W., Shinohara, H., Kusakabe, M., Ohba, T., 2003. Formation of acid volcanic brines through interaction of magmatic gases, sea-water, and rock within the White Island volcanic-hydrothermal system, New Zealand. Special Publications-Society of Economic Geologists. 10, pp. 19–40 (ISBN: 978-1-629496-28-3).

Gresse, M., Vandemeulebrouck, J., Chiodini, G., Revil, A., Johnson, T.C., Ricci, T., Vilardo, G., Lebourg, T., Grangeon, J., Bascou, P., Metral, L., 2017. 3-D resistivity tomography of the Solfatara crater (Italy): implication for the multiphase flow structure of the shallow hydrothermal system. J. Geophys. Res. 122. https://doi.org/10.1002/2017JB014389.

Guest, J., Gaspar, J.L., Cole, P., Queiroz, G., Duncan, A.M., Wallenstein, N., Ferreira, T., Pacheco, J., 1999. Volcanic geology of Furnas Volcano, São Miguel, Azores. J. Volcanol. Geotherm. Res. 92:1–29. https://doi.org/10.1016/S0377-0273(99)00064-5.

Guest, J.E., Pacheco, J.M., Cole, P.D., Duncan, A.M., Wallenstein, N., Queiroz, G., Gaspar, J.L., Ferreira, T., 2015. The volcanic history of Furnas Volcano, São Miguel, Azores. In: Gaspar, J.L., Guest, J.E., Duncan, A.M., Barriga, F.J.A.S., Chester, D.K. (Eds.), Volcanic Geology of São Miguel Island (Azores Archipelago), Geological Society of London Memoir. 44:pp. 125–134. https://doi.org/10.1144/M44.9.

Heap, M.J., Lavallée, Y., Petrakova, L., Baud, P., Reuschle, T., Varley, N.R., Dingwell, D.B., 2014. Microstructural controls on the physical and mechanical properties of edifice-forming andesites at Volcán de Colima, Mexico. J. Geophys. Res. Solid Earth 119 (4):2925–2963. https://doi.org/10.1002/2013JB010521.

Heap, M.J., Kennedy, B.M., Pernin, N., Jacquemard, L., Baud, P., Farquharson, J.I., Mayer, K., 2015. Mechanical behaviour and failure modes in the Whakaari (White Island volcano) hydrothermal system, New Zealand. J. Volcanol. Geotherm. Res. 295:26–42. https://doi.org/10.1016/j.jvolgeores.2015.02.012.

Heap, M.J., Kennedy, B.M., Farquharson, J.I., Ashworth, J., Mayer, K., Letham-Brake, M., Siratovich, P., 2017. A multidisciplinary approach to quantify the permeability of the Whakaari/White Island volcanic hydrothermal system (Taupo Volcanic Zone, New Zealand). J. Volcanol. Geotherm. Res. 332:88–108. https://doi.org/10.1016/j.jvolgeores.2016.12.004.

Hedenquist, J.W., Simmons, S.F., Giggenbach, W.F., Eldridge, C.S., 1993. White Island, New Zealand, volcanic-hydrothermal system represents the geochemical environment of high-sulfidation Cu and Au ore deposition. Geology 21 (8):731–734. https://doi.org/10.1130/0091-7613.

Herman, R., 2001. An introduction to electrical resistivity in geophysics. Am. J. Phys. 69 (9), 943–962.

Honnorez, J.J., Alt, J.C., Humphris, S.E., Herzig, P.M., Miller, D.J., Becker, K., Brown, D., Bruegmann, G.E., Chiba, H., Fouquet, Y., Gemmell, J.B., Guerin, G., Hannington, M.D., Holm, N.G., Iturrino, G.J., Knott, R., Ludwig, R.J., Nakamura, K.-i., Petersen, S., Reysenbach, A.-L., Rona, P.A., Smith, S.E., Sturz, A.A., Tivey, M.K., Zhao, X., 1998. Vivi-section and autopsy of active and fossil hydrothermal alterations of basalt beneath and within the TAG hydrothermal mound. In: Herzig, P.M., Humphris, S.E., Miller, D.J., Zierenberg, R.A. (Eds.), TAG—Drilling an Active Hydrothermal System on a Sediment-Free Slow-Spreading Ridge, Site 957: Proceedings of the Ocean Drilling Program, Scientific Results. 158, pp. 231–254.

Houghton, B.F., Nairn, I.A., 1991. The 1976–1982 Strombolian and phreatomagmatic eruptions of White Island, New Zealand: eruptive and depositional mechanisms at a 'wet' volcano. Bull. Volcanol. 54 (1):25–49. https://doi.org/10.1007/BF00278204.

Jeffery, A.J., Gertisser, R., Driscoll, B.O., Pacheco, J., Whitley, S., Pimentel, A., Self, S., 2016. Temporal evolution of a post-caldera, mildly peralkaline magmatic system: Furnas volcano, São Miguel, Azores. Contrib. Mineral. Petrol. 171 (42). https://doi.org/10.1007/s00410-016-1235-y.

Johnson, T.C., Versteeg, R.J., Ward, A., Day-Lewis, F.D., Revil, A., 2010. Improved hydrogeophysical characterization and monitoring through high performance electrical geophysical modeling and inversion. Geophysics 75 (4):WA27–WA41. https://doi.org/10.1190/1.3475513.

Jonscher, A.K., 1981. A new understanding of the dielectric relaxation of solids. J. Mater. Sci. 16:2037–2060. https://doi.org/10.1007/BF00542364.

Keith, T.E., White, D.E., Beeson, M.H., 1978. Hydrothermal alteration and self-sealing in Y-7 and Y-8 drill holes in northern part of Upper Geyser Basin, Yellowstone National Park, Wyoming. US Geol. Surv. Prof. Paper. 1054, p. 26.

Kemna, A., Binley, A., Cassiani, G., Niederleithinger, E., Revil, A., Slater, L., Williams, K.H., Orozco, A.F., Haegel, F.H., Hoerdt, A., Kruschwitz, S., Leroux, V., Titov, K., Zimmermann, E., 2012. An overview of the spectral induced polarization method for near-surface applications. Near surface. Geophysics 10 (6):453–468. https://doi.org/10.3997/1873-0604.2012027.

Komori, S., Kagiyama, T., Hoshizumi, H., Takakura, S., Mimura, M., 2010. Vertical mapping of hydrothermal fluids and alteration from bulk conductivity: simple interpretation on the USDP-1 site, Unzen Volcano, SW Japan. J. Volcanol. Geotherm. Res. 198 (3–4):339–347 (15). https://doi.org/10.1016/j.jvolgeores.2010.09.019.

Kushnir, A.R., Martel, C., Bourdier, J.L., Heap, M.J., Reuschlé, T., Erdmann, S., Cholik, N., 2016. Probing permeability and microstructure: unravelling the role of a low-permeability dome on the explosivity of Merapi (Indonesia). J. Volcanol. Geotherm. Res. 316:56–71. https://doi.org/10.1016/j.jvolgeores.2016.02.012.

Lesmes, D.P., Frye, K.M., 2001. The influence of pore fluid chemistry on the complex conductivity and induced-polarization responses of Berea sandstone. J. Geophys. Res. 106 (B3), 4079–4090.

Lyklema, J., Dukhin, S., Shilov, V., 1983. The relaxation of the double layer around colloidal particles and the low-frequency dielectric dispersion. Part I: theoretical considerations. J. Electroanal. Chem. Interfacial Electrochem. 143:1–21. https://doi.org/10.1016/S0022-0728(83)80251-4.

Mansoor, N., Slater, L., 2007. Aquatic electrical resistivity imaging of shallow-water wetlands. Geophysics 72:F211–F221. https://doi.org/10.1190/1.2750667.

Marmoni, G.M., Martino, S., Heap, M.J., Reuschlé, T., 2017. Gravitational slope-deformation of a resurgent caldera: new insights from the mechanical behaviour of Mt. Nuovo tuffs (Ischia Island, Italy). J. Volcanol. Geotherm. Res. 345:1–20. https://doi.org/10.1016/j.jvolgeores.2017.07.019.

Mayer, K., Scheu, B., Gilg, H.A., Heap, M.J., Kennedy, B.M., Lavallée, Y., Dingwell, D.B., 2015. Experimental constraints on phreatic eruption processes at Whakaari (White Island volcano). J. Volcanol. Geotherm. Res. 302:150–162. https://doi.org/10.1016/j.jvolgeores.2015.06.014.

Mazot, A., 2005. Activité hydrothermale des volcans Kelud et Papandayan (Indonésie) et évaluation des flux de gaz carbonique. (PhD thesis). Université Libre de Bruxelles.

Michot, D., Zahra, T., Issifou, A., 2016. Nonstationarity of the electrical resistivity and soil moisture relationship in a heterogeneous soil system: a case study. Soil 2:241–255. https://doi.org/10.5194/soil-2-241-2016.

Moon, V., Bradshaw, J., Smith, R., de Lange, W., 2005. Geotechnical characterisation of stratocone crater wall sequences, White Island volcano, New Zealand. Eng. Geol. 81 (2):146–178. https://doi.org/10.1016/j.enggeo.2005.07.014.

Moore, R.B., 1990. Volcanic geology and eruption frequency, Saõ Miguel, Azores. Bull. Volcanol. 52:602–604. https://doi.org/10.1007/BF00301211.

Nielsen, M.E., Fisk, M.R., 2008. Data report: specific surface area and physical properties of subsurface basalt samples from the east flank of Juan de Fuca Ridge. and the Expedition 301 Scientists. In: Fisher, A.T., Urabe, T., Klaus, A. (Eds.), Proc. IODP, 301, College Station, TX. (Integrated Ocean Drilling Program Management International, Inc.) https://doi.org/10.2204/iodp.proc.301.205.

Niu, Q., Revil, A., Saidian, M., 2016a. Salinity influence of the complex surface conductivity of Portland sandstone. Geophysics 81 (2):D125–D140. https://doi.org/10.1190/GEO2015-0426.1.

Niu, Q., Prasad, M., Revil, A., Saidian, M., 2016b. Textural control on the quadrature conductivity of porous media. Geophysics 81 (5):E297–E309. https://doi.org/10.1190/GEO2015-0715.1.

Ohmoto, H., 1996. Formation of volcanogenic massive sulfide deposits—the Kuroko perspective. In: Vielreicher, R.M., Groves, D.I., Heinrich, C.A., Walshe, J.L. (Eds.), Ore Geology Reviews. Elsevier, Amsterdam, pp. 135–177.

Pola, A., Crosta, G., Fusi, N., Barberini, V., Norini, G., 2012. Influence of alteration on physical properties of volcanic rocks. Tectonophysics 566:67–86. https://doi.org/10.1016/j.tecto.2012.07.017.

Reid, M.E., 2004. Massive collapse of volcano edifices triggered by hydrothermal pressurization. Geology 32 (5):373–376. https://doi.org/10.1130/G20300.1.

Reid, M.E., Sisson, T.W., Brien, D.L., 2001. Volcano collapse promoted by hydrothermal alteration and edifice shape, Mount Rainier, Washington. Geology 29 (9):779–782. https://doi.org/10.1130/0091-7613.

Revil, A., 2012. Spectral induced polarization of shaly sands: influence of the electrical double layer. Water Resour. Res. 48:W02517. https://doi.org/10.1029/2011WR011260.

Revil, A., 2013. Effective conductivity and permittivity of unsaturated porous materials in the frequency range 1 mHz–1 GHz. Water Resour. Res. 49:306–327. https://doi.org/10.1029/2012WR012700.

Revil, A., Hermitte, D., Spangenberg, E., Cochémé, J.J., 2002. Electrical properties of zeolitized volcaniclastic materials. J. Geophys. Res. 107 (B8):2168. https://doi.org/10.1029/2001JB000599.

Revil, A., Johnson, T.C., Finizola, A., 2010. Three-dimensional resistivity tomography of Vulcan's forge, Vulcano Island, southern Italy. Geophys. Res. Lett. 37 (15). https://doi.org/10.1029/2010GL043983.

Revil, A., Kessouri, P., Torres-Verdín, C., 2014. Electrical conductivity, induced polarization, and permeability of the Fontainebleau sandstone. Geophysics 79 (5):D301–D318. https://doi.org/10.1190/GEO2017-0036.1.

Revil, A., Florsch, N., Mao, D., 2015a. Induced polarization response of porous media with metallic particles — part 1: a theory for disseminated semiconductors. Geophysics 80 (5):D525–D538. https://doi.org/10.1190/GEO2014-0577.1.

Revil, A., Abdel Aal, G.Z., Atekwana, E.A., Mao, D., Florsch, N., 2015b. Induced polarization response of porous media with metallic particles — part 2. Comparison with a broad database of experimental data. Geophysics 80 (5):D539–D552. https://doi.org/10.1190/GEO2014-0578.1.

Revil, A., Murugesu, M., Prasad, M., Le Breton, M., 2017a. Alteration of volcanic rocks: a new non-intrusive indicator based on induced polarization measurements. J. Volcanol. Geotherm. Res. 341:351–362. https://doi.org/10.1016/j.jvolgeores.2017.06.016.

Revil, A., Coperey, A., Shao, Z., Florsch, N., Fabricius, I.L., Deng, Y., Delsman, J.R., Pauw, P.S., Karaoulis, M., de Louw, P.G.B., van Baaren, E.S., Dabekaussen, W., Menkovic, A., Gunnink, J.L., 2017b. Complex conductivity of soils. Water Resour. Res. 53. https://doi.org/10.1002/2017WR020655.

Revil, A., Le Breton, M., Niu, Q., Wallin, E., Haskins, E., Thomas, D.M., 2017c. Induced polarization of volcanic rocks – 1. Surface versus quadrature conductivity. Geophys. J. Int. 208:826–844. https://doi.org/10.1093/gji/ggw444.

Revil, A., Coperey, A., Deng, Y., Cerepi, A., Seleznev, N., 2018. Complex conductivity of tight sandstones. Geophysics 83 (2):1–20. https://doi.org/10.1190/geo2017-0096.1.

Rosas-Carbajal, M., Komorowski, J.C., Nicollin, F., Gibert, D., 2016. Volcano electrical tomography unveils edifice collapse hazard linked to hydrothermal system structure and dynamics. Sci. Rep. 6 (29899). https://doi.org/10.1038/srep29899.

Schlumberger, C., 1920. Study of Underground Electrical Prospecting (Paris, 99 pp).

Schufle, J.A., 1959. Cation exchange and induced polarization. Geophysics 24 (1):164–166. https://doi.org/10.1190/1.1438556.

Seigel, H.O., 1959. Mathematical formulation and type curves for induced polarization. Geophysics 24:547–565. https://doi.org/10.1190/1.1438625.

Shea, T., Houghton, B.F., Gurioli, L., Cashman, K.V., Hammer, J.E., Hobden, B.J., 2010. Textural studies of vesicles in volcanic rocks: an integrated methodology. J. Volcanol. Geotherm. Res. 190 (3):271–289. https://doi.org/10.1016/j.jvolgeores.2009.12.003.

Silva, C., Viveiros, F., Ferreira, T., Gaspar, J.L., Allard, P., 2015. Diffuse soil emanations of radon and hazard implications at Furnas Volcano, São Miguel Island (Azores). In: Gaspar, J.L., Guest, J.E., Duncan, A.M., Barriga, F.J.A.S., Chester, D.K. (Eds.), Volcanic

Geology of S. Miguel Island (Azores archipelago). 44. Geological Society, London: pp. 197–211 (Memoirs). https://doi.org/10.1144/M44.15.

Slater, L., Glaser, D., 2003. Controls on induced-polarization in sandy unconsolidated sediments and application to aquifer characterization. Geophysics 68:1547–1558. https://doi.org/10.1190/1.1620628.

Soueid Ahmed, A., Revil, A., Byrdina, S., Coperey, A., Gailler, L., Grobbe, N., Viveiros, F., Silva, C., Jougnot, D., Ghorbani, A., Hogg, C., Kiyan, D., Rath, V., Heap, M.J., Grandis, H., Humaida, H., 2018a. 3D electrical conductivity tomography of volcanoes. (in press). J. Volcanol. Geotherm. Res. https://doi.org/10.1016/j.jvolgeores.2018.03.017.

Soueid Ahmed, A., Revil, A., Jardani, A., Chen, R., 2018b. Geostatistical inversion of induced polarization data. Geophysics 83 (3):1–18. https://doi.org/10.1190/GEO2017-0232.1.

Surono Jousset, P., Pallister, J., Boichu, M., Buongiorno, M.F., Budisantoso, A., Costa, F., Humaida, H., 2012. The 2010 explosive eruption of Java's Merapi volcano-a '100-year' event. J. Volcanol. Geotherm. Res. 241:121–135. https://doi.org/10.1016/j.jvolgeores.2012.06.018.

Tikhonov, A.N., Arsenin, V.Y., 1977. Solutions of Ill-Posed Problems. John Wiley & Sons, Washington https://doi.org/10.1137/1021044.

Usui, Y., Ogawa, Y., Aizawa, K., Hashimoto, T., Koyama, T., Kagiyama, T., 2016. Three-dimensional resistivity structure of Asama Volcano revealed by data-space magnetotelluric inversion using unstructured tetrahedral elements. Geophys. J. Int. 208 (3):1359–1372. https://doi.org/10.1093/gji/ggw459.

Van Voorhis, G.D., Nelson, P.H., Drake, T.L., 1973. Complex resistivity spectra of porphyry copper mineralization. Geophysics 38 (1):49–60. https://doi.org/10.1190/1.1440333.

Vinegar, H.J., Waxman, M.H., 1984. Induced polarization of shaly sands. Geophysics 49: 1267–1287. https://doi.org/10.1190/1.1441755.

Viveiros, F., Cardellini, C., Ferreira, T., Caliro, S., Chiodini, G., Silva, C., 2010. Soil CO_2 emissions at Furnas volcano, São Miguel Island, Azores archipelago: volcano monitoring perspectives, geomorphologic studies, and land use planning application. J. Geophys. Res. 115:B12208. https://doi.org/10.1029/2010JB007555.

Voight, B., Constantine, E.K., Siswowidjoyo, S., Torley, R., 2000. Historical eruptions of Merapi volcano, central Java, Indonesia, 1768–1998. J. Volcanol. Geotherm. Res. 100 (1):69–138. https://doi.org/10.1016/S0377-0273(00)00134-7.

Waxman, M.H., Smits, L.J.M., 1968. Electrical conductivities in oil bearing shaly sands. Soc. Pet. Eng. J. 243:107–122. https://doi.org/10.2118/1863-A.

Wyering, L.D., Villeneuve, M.C., Wallis, I.C., Siratovich, P.A., Kennedy, B.M., Gravley, D.M., Cant, J.L., 2014. Mechanical and physical properties of hydrothermally altered rocks, Taupo Volcanic Zone, New Zealand. J. Volcanol. Geotherm. Res. 288:76–93. https://doi.org/10.1016/j.jvolgeores.2014.10.008.

Zimmermann, E., Kemna, A., Berwix, J., Glaas, W., Munch, H., Huisman, J., 2008. A high-accuracy impedance spectrometer for measuring sediments with low polarizability. Meas. Sci. Technol. 19 (10):105603. https://doi.org/10.1088/0957-0233/19/10/105603.